공학박사학위논문

회전이 입자상 재밍에 미치는 영향: 회전하여 자가매립하는 씨앗에서 착안한 연구

Effects of rotation on granular jamming: a study inspired by self-burrowing seeds

2017 년 2 월

서울대학교 대학원

기계항공공학부

정 원 종

Effects of rotation on granular jamming: a study inspired by self-burrowing seeds

Wonjong Jung
Department of Mechanical and Aerospace Engineering
Seoul National University

A thesis submitted for the degree of
Doctor of Philosophy

February 2017

Abstract

Effects of rotation on granular jamming: a study inspired by self-burrowing seeds

Wonjong Jung
Department of Mechanical and Aerospace Engineering
The Graduate School
Seoul National University

In the presented thesis, we conducted experimental and mathematical analysis of the effects of rotation on granular jamming, which is inspired by self-burrowing rotary seeds. Based on the results of the drag reduction by seed's spinning in granular media, we experimentally revealed that rotational motion impede the formation of force chain network near the intruder by inducing local slip motion of grains, leading the reduction of the effective area where granular hydrostatic acts. In addition, we found a semi-empirical model for the drag reduction depending on the relative slip velocity of grains by rotation, which showed a good agreement with the experimental results. To validate this physical model, we newly provided a noble and effective technique to investigate the internal jamming process in granular medium using the electrically conductive particles. This study can provide an advanced insight into how grain rearrangements in a localized region can significantly weaken the drag force in granular media.

We first introduced the self-burrowing rotary seeds, which is a motivation of this study. We present the results of a combined experimental and theoretical investigation of the mechanics of self-burial of some plant seeds whose morphologies respond to environmental changes in humidity. The seeds of *Erodium* and *Pelargonium* have hygroscopically responsive awns that play a critical role in their self-burial into soil. The awn, initially coiled in a dry state, uncoils to stretch linearly under highly humid condition because of a tilted arrangement of cellulose microfibrils in one of the layers of the awn's bilayered structure. By measuring the mechanical characteristics of the awns of *Pelargonium carnosum*, we found that the extensional force of the awn can be aptly modeled by the theory of elasticity for a coiled spring. We further showed that although the resistance to the seed-head penetrating relatively coarse soils without spinning is large enough to block the digging seed, the rotation of the seed greatly reduces the soil's resistance down to a level the awn can easily overcome. Our mechanical analysis reveals that the self-burial of the seed is a sophisticated outcome of the helically coiled configuration of the awn.

Next, we studied the drag force for the slowly moving intruder whose speed is comparable with the penetrating speed of the self-burrowing seeds in soil. The drag force acting on the intruder is determined by the inertial number I, which can be estimated by the importance of the dynamic friction relative to the static friction in granular media. In quasi-static flow regime ($I < 10^{-3}$), the static friction resulted from the granular hydrostatic pressure mainly responsible for the drag force. We measured the drag forces for the vertically penetrating intruders in granular medium, and found that the granular hydrostatic pressure normally acts on the intruder. In addition, we investigated the effects of the grain size polydispersity and the relative

size of grain to the intruder on the granular drag in quasi-static flow regime.

We next presented quantitative measurements and mathematical analysis of the granular drag reduction by rotation, as motivated by self-digging of *Erodium* and *Pelargonium* seeds. The seeds create an extensional motion with rotation to dig into soil before germination using their moisture-responsive awns, which are originally helical shaped but reversibly deform to a linear configuration in a humid environment. We showed that the rotation greatly lowers the resistance of soil against penetration because grain rearrangements near the intruder change the force chain network. We found a general correlation for the drag reduction by relative slip of grains, leading to a mathematical model for the granular drag of a rotating intruder. In addition to shedding light on the mechanics of rotating body in granular media, this work can guide us to design robots working in granular media with enhanced maneuverability.

To validate the rearrangement of the force chains by rotation of the intruder, we provided a noble technique to investigate the internal jamming in granular media. Granular jamming is determined by the force chain which consists of contacts between neighboring grains. Under jamming, the electrically conductive particles forms the electrical current paths along with the force chains. Based on the intuitive consideration, we experimentally measured the electrical resistance of granular medium consisting of the electrically conductive particles, solder balls, while trusting an intruder with rotation and without rotation. We found that the electrical resistance decreases with the burial depth, and the reduction behavior of the electrical resistance is delayed as increasing the rotational speed indicating that the effective area, which is supported by the granular force chains,

is reduced by rotation. This work brings the complicated granular jamming down to a comprehensible level and gives a new shortcut to fabricate sustainable digging robots.

Keywords :Granular material, granular drag, jamming, botanical movement, self-burrowing seeds, hygroscopic material
Student Number : 2013-30211

Contents

List of Figures

List of Tables

Chapter 1

Introduction

1.1 Outline

Motivated by the self-burrowing rotary seeds, the aim of this thesis is to elucidate the effects of rotation on drag force and jamming in granular media. In chapter 1, we deal with the backgrounds for hygroscopic botanical motion and drag force in granular media. The presented thesis is largely divided into two parts. The first part covers the mechanics of the self-burrowing rotary seeds in chapter 2. The second part covers the vertical granular drag in quasi-static flow regime in chapter 3 and the granular drag reduction by rotation in chapter 4-5.

In the first part, we investigate the mechanics of the self-burrowing seed with hygroscopically responsive awn, which create a helical motion in response to changes in environmental humidity. They generate a thrust with rotation against soil, so that a helical motion enables the seed to dig into the ground. We note that the rotational motion of the seed head greatly reduce the soil's resistance. Motivated by the self-burrowing rotary seeds, we investigate the reduction of the granular drag by rotation in the second part. We first study various characteristics of the granular drag force for the vertically penetrating intruder in quasi-static flow regime in chapter 3. We experimentally demonstrate the granular drag increases with the burial depth and normally acts on the intruder surface. Based on these results,

we then investigate the drag reduction by rotation in chapter 4. We show that the rotation greatly lowers the magnitude of the drag force, but not change the dependency on the burial depth, leading a mathematical model to describe the drag reduction by rotation. In the last chapter 5 of the second part, we newly provide a noble technique to investigate granular jamming using the electrically conductive particles. We experimentally show the relaxation of the force chain network near the intruder by rotation via measuring the electrical resistance of granular medium consisting of the electrically conductive particles. In the end of this thesis, we present concluding remarks in chapter 6, where we provide the summary and future work.

1.2 Backgrounds

1.2.1 Hygroscopic botanical motion

It is difficult to notice motions in plants, because their motion occurs in a large time scale and a passive way. Despite of lack of muscles and a central of nervous system, botanical motion can be evident by following examples: folding of *Mimosa* leaves (Weintraub, 1952), snapping of Venus flytraps (Foreterre *et al.*, 2005), blooming flowers, and opening of a pine cone (Reyssat *et al.*, 2009). Especially, the opening of a pine cone is water-driven botanical deformation which is called as hygroscopically responsive deformation. Cellulose fiber and hydrogel is representative hygroscopic materials which generally have a hydrophilic moiety allowing water molecules to be stored between the intermolecular chain network of cellulose fiber and hydrogel via hydrogen bonding. The volume between intermolecular chains increases as they become absorbed by water molecules, leading to swelling of wet tissues. As drying, they reversibly shrink back to its original size. Swelling sponge and buckling of wet paper with imbibition (Lee *et al.*, 2016) are also hygroscopically responsive deformations.

Surprisingly, some plants use such hygroscopic response of seeds for self-burrowing. Wild wheat has a pair of awns which are hygroscopically

responsive and linear appendages of the seeds. The awn of wild wheat consist of two different layers: hygroscopically inactive and active layer. Therefore, the difference in expansiveness causes the bending of the awn, which repeats as the changes in environmental humidity (Elbaum *et al.*, 2007). The bending motion enables the seed head to dig into the soil, granular media, and to find a favorable site for germination. *Erodium* and *Pelargonium*, the family of Geraniaceae, exhibit relatively complicate motions which play a crucial role in seed dispersal and burial (Abraham & Elbaum, 2013a; Evangelista *et al.*, 2011; Jung *et al.*, 2014; Stamp, 1984). The seed-dispersal unit of *Erodium* and *Pelargonium* has a helically coiled awn consisting hygroscoipically responsive tissue. The hygroscopically responsive awn spontaneously coils in dry environment, while it is linearly stretched out in humid environment. Such reversible helical motions generate elastic energy being catapulted from the mother plant and drilling forces for self-burial.

We have two questions for the hygroscopically responsive awns. How large are the forces they generate? What is the role of seed's sinning induced by the helical deformation of the awn? To find the answers, we model the mechanics of self-burial. The force generated by hygroscopic deformation of the awn is related to two different types of deformations: a trust by awn spring extension and a torque by awn-tail rotation. The detailed mechanics of the hygroscopic deformation of the awn will be followed in chapter 2.

1.2.2 Drag force in granular materials

Granular material is the second-most-handled material in industry, second only to water (Richard *et al.*, 2005). For examples, pharmaceutical, food, powders, mechanosynthesis, semiconductor industries and geological science deeply deal with granular materials and particulate systems (see Fig. 1.1). The analysis of granular behaviors has several difficulties due to lack of constitutive equations like Navier-Stokes equations in fluid mechanics (Forterre & Pouliquen, 2008). Jamming (Cates *et al.*, 1998) and Brazil nut effect (Shinbrot, 2004) are the representative examples which are not

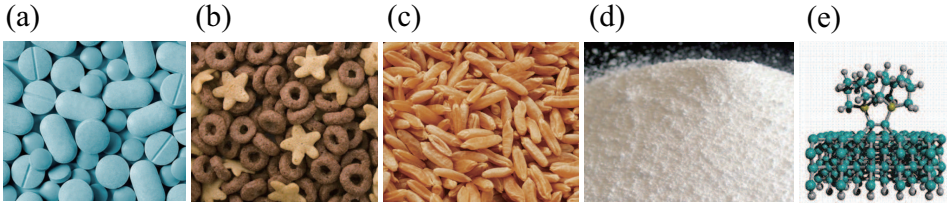

Figure 1.1: Examples of granular materials. Aggregates of pills (a), cereals (b), grain crops (c), powders (d), and molecules (e).

easily analysed by classical fluid mechanics. To understand the behaviors of granular system, granular flow is divided into three flow regimes: a dense quasi-static flow, intermediate liquid flow, and gaseous flow regimes. These three flow regimes can be easily observed in a hourglass at the same time (Wu *et al.*, 1993). The sand grains in upper glass chamber is stationary like solid (quasi-static flow), and the sand grains begin to flow through the hourglass nozzle like liquid (liquid flow) into the lower glass chamber where the sand grains collide with each others or a sand pile like gas phase (gaseous flow).

Transition from quasi-static to liquid flow is determined by the internal friction coefficient $\mu = \tan\theta$, where θ is an angle of repose of a granular pile (Jaeger & Nagel, 1996). Above the critical angle, grains flows along the slope of granular pile. However, grains under the critical angle are motionless, and support the granular pile forming the force chain networks. This threshold angle is reminiscent with yield stress in Bingham fluid, indicating that an internal stress exists in granular medium. In addition, the internal friction coefficient μ depends on the shear rate and shows a hysteresis behavior. Because of these reasons, rheological approaches have been made to describe granular flow, leading the dimensionless number $I = \dot{\gamma} d/(P/\rho)^{1/2}$ called as the inertial number, where $\dot{\gamma}$ is the shear rate, d is the grain diameter, P is the pressure, and ρ is the grain density (MiDi, 2004). The inertial number I is the ratio between two time scales: the microscopic time scale $d/(P/\rho)^{1/2}$ and the macroscopic time scale $1/\dot{\gamma}$. Granular flow generally can be classified by the inertial number I as following: quasi-static

flow ($I < 10^{-3}$), liquid flow ($10^{-3} < I < 10^{-1}$), and gaseous flow regimes ($I > 10^{-1}$) (Forterre & Pouliquen, 2008).

Granular drag is one of the most interesting area in granular mechanics. In low velocity regime, granular drag is described as the force required to collapse the force chains that determine the jammed state occurring in granular bulk (Albert *et al.*, 2000, 2001a, 1999). Besides, frictional characteristics like stick-slip behavior, that is common feature in solid contact mechanics, is naturally observed in the granular drag (Albert *et al.*, 2001b). The granular drag for the horizontally moving intruder can be estimated by the product of the characteristic size of the intruder and the immersed depth. However, the drag force is independent of the velocity and surface properties of the intruder. In case of vertical penetration of the intruder, granular drag is also scaled with the intruder size and the immersed depth, and independent of the moving velocity of the intruder and the grain size (Brzinski III *et al.*, 2013; Hill *et al.*, 2005; Stone *et al.*, 2004).

Rotating intruder also experiences the drag force in granular media. When an object slowly rotates at a given depth in granular medium, the measured torque is almost constant and independent of the rotational speed (Brzinski III & Durian, 2010). Interestingly, when a rod rotates horizontally with slow rotational speed, it disturbs the arrangement of the jammed grains, so that the rotational torque dramatically decreases after half a turn at a given depth (Guillard *et al.*, 2013). Using a rheometer instrument, various effects of particle size and fluid viscosity on granular drag induced by a rotating vane is studied by Higashi et al. (Higashi & Sumita, 2009). Despite of the experimental studies on granular drag acting on the rotating intruder, understanding of the drag force for a vertically penetrating rotary intruder remains incomplete due to complicated intergranular mechanics.

We present experimental results and a mathematical model to describe the granular drag reduction by rotation in chapter 3-4. We found that rotation promote the local slip of grains near the intruder leading the reduction of drag force. To validate this model, we provide a noble method

to investigate the relaxation of the force chain networks by rotation using the electrically conductive particles in chapter 5.

Chapter 2

Self-burial mechanics of hygroscopically responsive awn

2.1 Introduction

Plants can generate motions and deformations, that our eyes often fail to catch, in response to various stimuli such as light, heat, gravity, and change in humidity. Slow movements of plants are evidenced by twirling circumnutation of growing tendrils (Gerbode *et al.*, 2012) and blooming flowers (Reyssat *et al.*, 2009), whereas motions rapid enough to notice include dispersal of seeds of Dwarf mistletoe (Hinds & Hawsworth, 2000), folding of *Mimosa* leaves (Weintraub, 1952), and snapping of Venus flytraps (Foreterre *et al.*, 2005). A remarkable common feature in strategies of these motions is that they do not rely on complicated protein structures like muscles. Instead, most botanical movements are hydraulic in nature-that is, simple transport of fluid consisting mostly of water into and out of plant tissue generates motions. Also, such motions are often triggered by supply of deprival of water either in the form of liquid or vapor.

A common example of water-driven botanical deformation is the opening and closing pine cones in response to environmental changes in humidity,

whose mimic was built by layering hygroscopically active and inactive films (Reyssat *et al.*, 2009). It is now widely known that seeds and spores of some plant and fungus species are explosively launched into the air as their ovaries and sporophores, respectively, become exceedingly dry and crack open (Beer & D., 1977; Dumais & Forterre, 2012; Lee *et al.*, 2005). A pair of awns of wild wheat (*Triticum turgidum* ssp. *dicoccoides*) repeatedly open and close on the ground in response to variation of the soil's moisture content, which is a remarkable motion seeds employ in self-burial (Elbaum *et al.*, 2007). Ma et al. (Ma *et al.*, 2013) showed that an engineered, hygroscopically active film can be actuated by a humidity gradient in the surrounding air, just as are the awns of wild wheat. This process potentially can be used to generate electricity if piezoelectric properties are effectively combined.

Among various kinds of botanical motilities driven by change in humidity, here we aim to analyze the motions of seeds of some species of the genera *Erodium* and *Pelargonium*. It was revealed several decades ago that the seed of *Erodium cicutarium* has a helical awn that spontaneously uncoils when wet but re-coils when dry (Stamp, 1984). Such hygroscopic characteristics are known to play a critical role both in dispersal and germination of seeds. In a dry season, the seeds of *E. cicutarium*, confined in straight configuration in an ovary, are explosively launched into air as the ovary shell cracks due to low humidity. The mechanical energy stored in the awn is released rapidly as it coils to turn to its natural shape when in the dry state. A physical model of this process was developed by Evangelista et al. (Evangelista *et al.*, 2011). The helical configuration of dry *E. cicutarium* seeds was mathematically described using a non-euclidean rod-model by Aharoni et al. (Aharoni *et al.*, 2012). Upon landing, the seeds screw into the ground with the coiling and uncoiling cycle of the awn, a self-burial behavior different from that of wild wheat.

The awns of *Pelargonium*, another genus of the family Geraniaceae, to which *Erodium* belongs, also coil and uncoil in response to changes in humidity as demonstrated by a seed of *Pelargonium carnosum* in Fig. 2.1

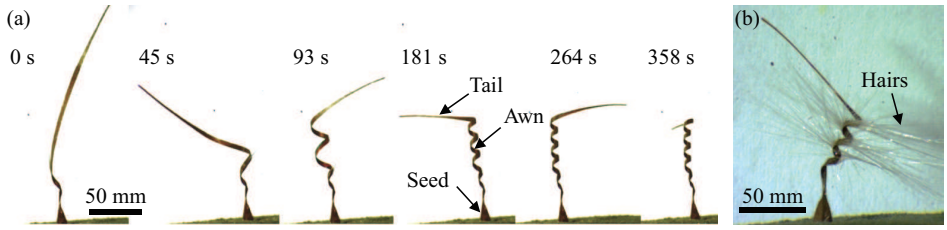

Figure 2.1: (*a*) Helical coiling of an awn of *Pelargonium carnosum* that is dried at room temperature from the initially wet, straight configuration. (*b*) A parachute-like shape of a *P. hortorum* seed with hairs.

(a). However, the awns of *Pelargonium* typically are thinner and softer than those of *Erodium* species. It is because their seeds become airborne by lift from wind rather than being catapulted like *Erodium* seeds (Abraham & Elbaum, 2013b). Thus, the seeds of *Pelargoium* are relatively light and covered with feather-like hairs, so that the seeds serve as parachutes when dry (Fig. 2.1 (b)). Therefore, the helical motion itself does not drive the release of the seeds in *Pelargonium*. Rather, the helical motion of the awns *Pelargonium* is mainly used to screw the seeds into ground. Therefore, the microstructure and shape of the seeds of *Pelargonium* are highly likely to have been evolved within the context of self-burial exclusively, not for dispersal. Below we provide physical accounts of hygroscopically driven botanical movements, which particularly lead to helical coiling and uncoiling of the awns of seeds. We also present experimental results for mechanical properties of some seeds of *Pelargonium* that enable their unique self-burial behavior. Investigating the water-driven helical motion of the awns can contribute to development of micro-robot actuators powered by environmental changes in humidity, as well as advancing and diversifying our understanding of botanical movements.

2.2 Mechanisms and geometry of botanical movements

In general, there are two different mechanisms that generate botanical motions or deformations. In some plants, the creation of motion relies on changes in turgor pressure, which is caused by the osmotic flow of water through plasma membranes, as driven by a gradient in concentration of solute. Increased turgor pressure inflates the membrane against the cell wall, thus providing the rigidity of the plant's organ. Plants may actively control solute concentration and thereby generate motions, such as the opening of stomata (Franks *et al.*, 2001), blooming and wilting of flowers, folding of *Mimosa* leaves, and closing of Venus flytraps. A similar role of turgor pressure can be observed in the kingdom of fungi; fungal spores are ejected from mushrooms due to the osmotic pressure and turgid tissues (Roper *et al.*, 2010).

Besides changes of turgor pressure due to osmosis, many motions of plants are caused by volumetric change owing to the hygroscopic nature of some constituent materials. The wall of plant cells is a composite made up of cellulose microfibrils and the soft matrix inside the cell walls expands when it combines with molecules of water. Hygroscopic materials generally have hydrophilic moiety, allowing water molecules to be stored between intermolecular chains or networks via hydrogen bonding. The volume between intermolecular chains or networks increases as they become impregnated by water molecules, leading to swelling of wet tissue. Because the combination with water molecules is reversible, the plant's swollen tissue can shrink back to its original size when dry. Such hygroscopic response is responsible for the opening of pine cones (Reyssat *et al.*, 2009), self-sealing of pollen grains (Katifori *et al.*, 2010), opening of seed pods (Armon *et al.*, 2011), and self-burial of the awns (Stamp, 1984).

The geometry of deformed plant tissues after hygroscopic expansion is often determined by the arrangement of microfibrils, fiber-like strands consisting of glycoproteins and cellulose. Because the water-driven swelling of

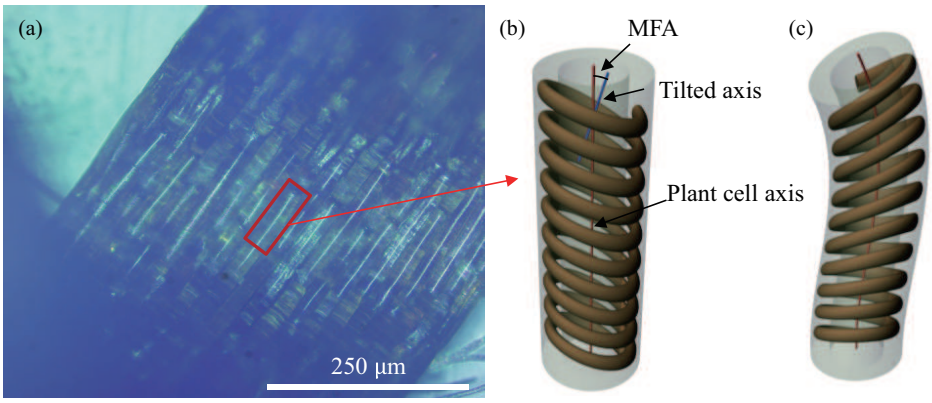

Figure 2.2: The optical image of the inner layer of the awn of a *Pelargonium carnosum* seed (*a*). The schematic illustration of a tilted helix of microfibril along the plant cell, depicted a in Fig. 5 of Abraham et al. (Abraham *et al.*, 2012) (*b*). Bending and twisting occur in the awn as it dries (*c*).

plant cell walls occurs in the hygroscopic soft matrix between crystalline cellulose fibrils, the direction of the hygroscopic swelling is perpendicular to the orientation of cellulose microfibrils. Attaching multiple layers of differently arranged microfibrils can yield bending or twisting of the structure. Indeed, hygroscopic tissues found in awns of wild wheat, *Erodium* and *Pelargonium* seeds typically consist of multiple layers with different orientations of their microfibrils.

The awns of wild wheat consist of two layers, called a ridge layer and a cap layer. While a ridge layer has randomly oriented cellulose microfibrils, in the cap layer the cellulose microfibrils are well aligned along the long axis of the cell (Elbaum *et al.*, 2007, 2008). Because the direction of primary expansion is orthogonal to the arrangement of cellulose microfibrils, the ridge and cap layers have a longitudinal expansion and a two-direction expansion in a plane, respectively. The difference in expansion causes the bending of the awn, which repeats as the environmental humidity changes. This motion enables the seed to employ silicified ratchets to dig into the soil and to find a place advantageous for germination.

The awns of *Erodium* and *Pelargonium* exhibit deformation distin-

guished from that of wild wheat by coiling helically rather than merely bending. A fully wet awn of *E. cicutarium* is straight, but it transforms to a helical coil when dry. The helical configuration is defined by the microfibril angle (MFA), the angle between the long axis of the plant cell and the axis perpendicular to the plane formed by the microfibrils (Barnett & Bonham, 2004). Because the cell wall contracts in a direction essentially perpendicular to the plane formed by the microfibrils, the direction of contraction is determined by the MFA (Fratzl *et al.*, 2008). When cellulose microfibrils are helically coiled along the plant cell at a tilted angle, hygroscopic deformation induces twisting as well as bending (Abraham & Elbaum, 2013a; Abraham *et al.*, 2012). The inner layer of the awn of *Pelargonium* is shown in Fig. 2.2.

2.3 Theory of the force generated by self-burrowing seeds

To investigate the forces generated by self-burrowing seeds, we begin with a brief description of the mechanics of the bending of a beam (Landau & Lifshitz, 1970). When loads are applied to a straight beam in the direction perpendicular to the longitudinal axis of the beam, the beam bends in a curve. A curve can be geometrically described in terms of curvature κ or the radius of curvature $\rho = 1/\kappa$. Because bending a straight beam induces the relative rotation $\mathrm{d}\theta$ of two cross-sections that are separated by an infinitesimal distance $\mathrm{d}s$ as shown in Fig. 2.3, we get $\mathrm{d}s = \rho \mathrm{d}\theta$. The strain ϵ, the ratio of the elongated length to the original length, depends on the distance y from the neutral surface in which longitudinal lines do not change in length, such that $\epsilon \approx \kappa y$.

The relationship between the curvature and loads can be deduced by the strain-stress relationship in elastic material: Hooke's law. In elementary solid mechanics, the moment-curvature relation is given by $M = EI\kappa$, where M is the local bending moment produced by the external loads, E is Young's modulus, and I is the area moment of inertia. Note that bending

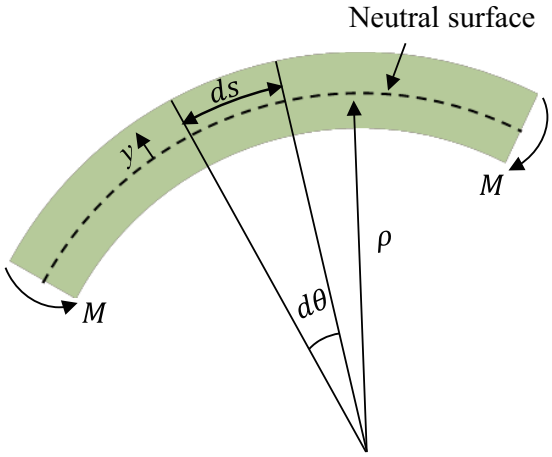

Figure 2.3: A beam subjected to a bending moment M.

stiffness EI is given by a combination of material property E and geometric characteristic I that depends on the cross-sectional shape of the beam, A beam with a rectangular cross-section has $I = bh^3/12$, where b and h are the width and the height of the cross-section, respectively. If a beam is originally curved, the applied moments produce the change in curvature, such that $M = EI\Delta\kappa$ when a small deflection is assumed.

The curvature of hygroscopic awns may change via the spatial variation of the degree of expansion. When two different layers of an awn differ in strain $\Delta\epsilon$ after hygroscopic expansion, the curvature is given by $\kappa\ \Delta\epsilon/t$, where t is the characteristic thickness of the awn. As deformation of one layer is restricted by the other, the difference in curvature between the natural and restricted configurations, $\Delta\kappa$, results in a bending moment on the other layer. Although a beam consisting of two rectangular layers with uniform cross-sections exhibits two-dimensional deformation, a beam of two non-rectangular layers can bend in a three-dimensional fashion because of asymmetry in deformaion. Jeong et al. (Jeong *et al.*, 2011) demonstrated that a planar structure with a sloped bilayer is bent as well as twisted when one of the layers is asymmetrically expanded. Because the ratio of two layers varies with the distance b, which results in a three dimensional deformation (see Fig. 2.4 (a))

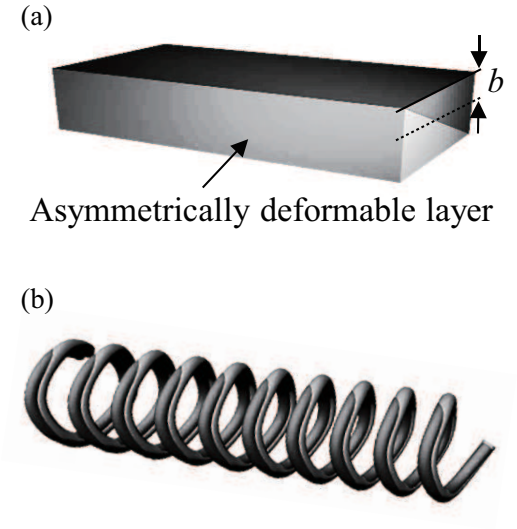

Figure 2.4: A bilayer with asymmetrically deformable layer (a). Shrinking and consequent twsting in a spiral of the bilayer (b). The figures is depicted as in Fig. 3 of Jeong et al. (Jeong *et al.*, 2011).

In the case of the awns of *Erodium* and *Pelargonium* seeds, a single layer, referred to as an inner layer, consists of a number of cells, each of which is capable of bending and twisting as shown in Fig. 2.4.The soft matrix of the cell wall contracts when dry, but the cell wall is wound around by hygroscopically inactive microfibrils. Therefore, the cell can contract only in the direction perpendicular to the plane formed by the rotation of microfibrils (Fratzl *et al.*, 2008). Because the direction of contraction does not coincide with the long axis of the cell, the cell must bend and twist while drying. A simple hybrid beam is shown in Fig. 2.4 and the cells of interest here share a common feature in that they coil due to different hygroscopic responses of the two constituent materials. The difference lies in the spatial arrangement of the materials-the simple hybrid beam has completely separated layers of hygroscopically active and inactive microfibrils are embedded in and twined around the hygroactive materilas of the cell. The helical deformation of the inner layer of the awn is the collective outcome of its constituent cells' deformations. On the other hand, the outer

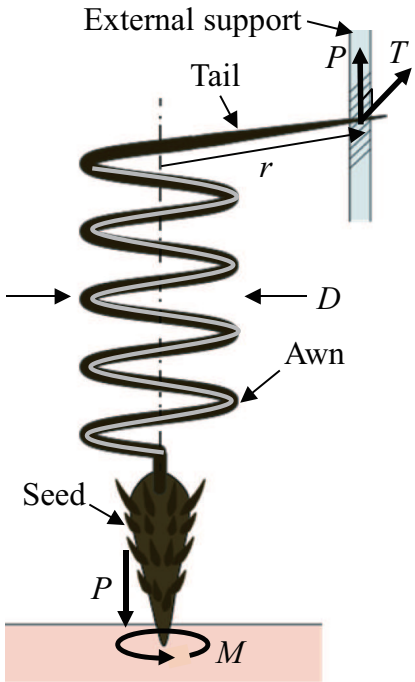

Figure 2.5: Geometry and forces of a seed with a helically coiled awn digging into soil. The arrows of P and T are perpendicular to each other.

layer contributes to the coiling of the awn but slightly because its cells have smaller MFA than the inner layer. Therefore, the inner layer plays a pivotal role in the helical deformation of the awn whereas the outer layer passively modifies the degree of deformation (Abraham & Elbaum, 2013a).

Coiling and uncoiling of the awns of *Erodium* and *Pelargonium* seeds result in rotation and consequent digging by the seeds. Digging arises from two different mechanical effects: force due to coil expansion and torque due to awn-tail rotation. The forces are exerted against a support provided by pebbles or bark of trees in nature (Stamp, 1984), as schematically illustrated in Fig. 2.5. Uncoiling of a helical structure into a straight configuration leads to a change in length along the axis of the helix, and thrust (P) is exerted normal to the surface of the soil. In addition, the relative rotation of the helical structure to the tip of the long tail produces torques ($M = rT$). The thrust and torque together are responsible for self-burial of the seed.

The order of magnitude of force generated by the coiling deformation can be estimated from a coiled-spring model. For a linear coil spring with rectangular cross-section, the displacement δ under axial loading P is given by $\delta\ PlD^2/(EI)$, where l is the length of the anctive wire of the spring (the length of the gray line in Fig. 2.5) and D is the diameter of the coil (**?**). Therefore, the spring constant K, i.e., loading per unit displacement, is estimated as

$$K \sim EI\kappa^2/l. \tag{2.1}$$

We see that the coil can generate a larger force (high K) with the same displacement as the coil becomes stiffer, thicker, more highly curved and shorter. One should note that while the linear coil spring model assumes constant E, I, and curvature, and thus a constant moment along the length, the actual awn experiences changes in E, I, and curvature both spatially and temporally as the environmental humidity varies. More sophisticated models, for example a logarithmic spiral model for a helix (Evangelista *et al.*, 2011) and a variable stiffness model due to moisture diffusion in the tissue (Reyssat *et al.*, 2009), can allow us to predict the spring force more accurately, which we do not pursue further here. For the seed to dig into the ground, the thrust generated by the helical coil should overcome the resistance of the soil to penetration. Below, we experimentally measure the forces produced by the self-burrowing seeds and compare the results with both the theoretical values and the soil's resistance.

2.4 Materials and methods

2.4.1 The seeds of *Pelargonium carnosum*

The seeds were purchased from a nursery (Phoenix Desert Nursery) in AZ, USA, and their shapes are displayed in Fig. 2.6. The SEM image (Fig. 2.6 (b)) was taken after sputter-coating the specimen with Pt. In the following, we present the average values of the seeds' dimensions through

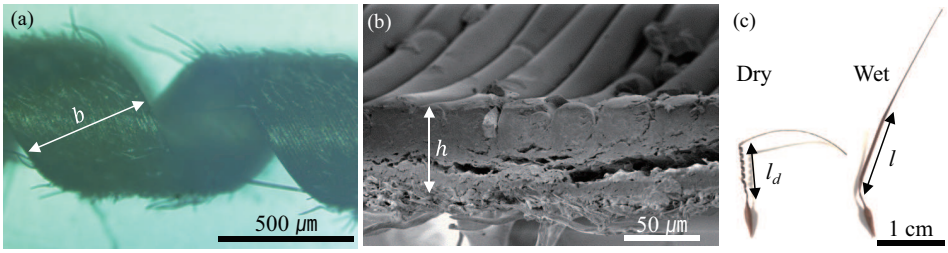

Figure 2.6: The awn of *Pelargonium carnosum*. (a) Optical micrograph of the coiled awn. (b) SEM image of the cross-section. (c)Optical images of the seed in dry and wet states.

measurements of n specimens. The seed head of *P. carnosum* is 5.3 ± 0.3 mm long and the tail length of the awn is 19.5 ± 1.3 mm ($n = 3$). The end-to-end distance of dried awn $l_d = 8.7 \pm 0.3$ mm, the length of wet awn $l = 15.0 \pm 1.3$ mm, the maximum width of the awn $b = 531 \pm 66$ μm, the height of the cross section of the awn $h = 51 \pm 7.6$ μm ($n = 3$), when hairs were removed before measurement. The maximum coil diameter of the awn is $D = 1.0 \pm 0.2$ mm, the mass of seed without hairs is 4.3 ± 0.5 mg, and the number of turns in a completely dried state is 7 ± 1 ($n = 10$). Assuming that Young's modulus of the awn of *P. carnosum* to be similar to that of wood in a direction parallel to the grain, $E \sim 9$ GPa **?**, the spring constant K of the awn of *P. carnosum* seeds is estimated from Equation (1) to be ~ 12.5 N/m. Here, we used $I = bh^3/12 = 5.2 \times 10^{-18}$ m^4 and $\kappa = 2/D = 2 \times 10^3$ m^{-1}.

2.4.2 The measurement of forces generated by the awn

In order to measure the forces generated by the deformation of the awn, we used a load cell originally intended for measurement of dynamic contact angle (DCA 21, DataPhysics instruments GmbH). Humidity around the awn was increased by supplying vapor in the surrounding air with a commercial humidifier. One end of the awn was fixed to an external support, and the other (free) end was located within 1 mm from the load cell (Fig. 2.7 (a) and 2.8 (a)). As we increased humidity, the initially

free end of the awn touched and pushed the load cell. The extensional force was measured by constraining the increase in length as shown in Fig. 2.7 (a) and the torque was measured by obstructing the rotation as shown in Fig. 2.8 (a). The forces produced by three different awns of *P. carnosum* were measured in each measurement. The scatter in the values of measurements among the specimens was most ±50% from the data of the specimen shown following. Since we are interested in obtaining estimates of the forces generated by the awn, only to the order of magnitude, the observed variability of the force data does not invalidate the simple mechanical model constructed in this work.

2.4.3 The measurement of forces required for digging

In order to measure the thrust forces required for the seed of *P. carnosum* to dig into soil, we also used the load cell system of DCAT 21. Various sizes of glass beads (SiLibeads, Sigmund Linder GmbH) were used to mimic the soils in nature. One end of the seed head was fixed to the load cell and a beaker containing the glass beads moved against the seed with a constant velocity of 0.05 mm/s (Fig. 2.9 (a)). In experiments to measure the thrust forces during rotation of the seed, we rotated the beaker at 7 rpm while maintaining the linear constant speed of 0.05 mm/s this corresponds to the advance of the seed by the length of the seed head after 7 revolutions (equal to the number of turns of the awn). Five different seed heads were used for the measurement. The scatter of the values of the measurements among the specimens was at most ±50% from the data for the specimen shown here.

2.5 Experimental results

The forces produced by three awns of *P. carnosum* were measured as shown in Fig. 2.7 (a). Fig. 2.7 (b) presents representative measurements of the forces with respect to time. As the awn rotates during expansion, the contact of the end of the awn with the load cell is periodically loosened.

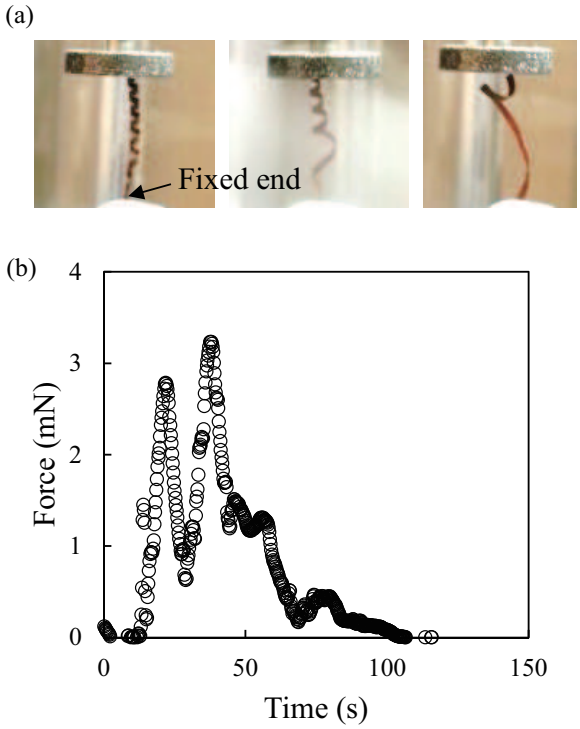

Figure 2.7: (a) Experimental set-up to measure the extension force of the awn of *Pelargonium carnosum*. (b) Measurements of the extension force.

Thus, the force measured by the load cell shows multiple peaks. The force peak reached at ~ 40 s is ~ 3.2 mN, at which instant the axial displacement is measured to be 0.5 mm. Although the awn stretches until the axial extension reaches ~ 6 mm (Fig. 2.7 (b)), the thrust does not monotonically increase with the extension. It is because Young's modulus dramatically decreased as the plant tissue becomes wet (Hepworth & Vincent, 1998) and the awn buckles when stretched exceedingly. The thrust predicted by the coiled-spring model when δ is 0.5 mm is $P = K\delta \sim 6$ mN, a value in reasonable agreement with the experimental measurement.

The deformation of the awn of *P. carnosum* produces rotational motion in addition to the axial expansion. When the awn's tail is fixed by an external means, the uncoiling motion of the awn induces the rotation of the

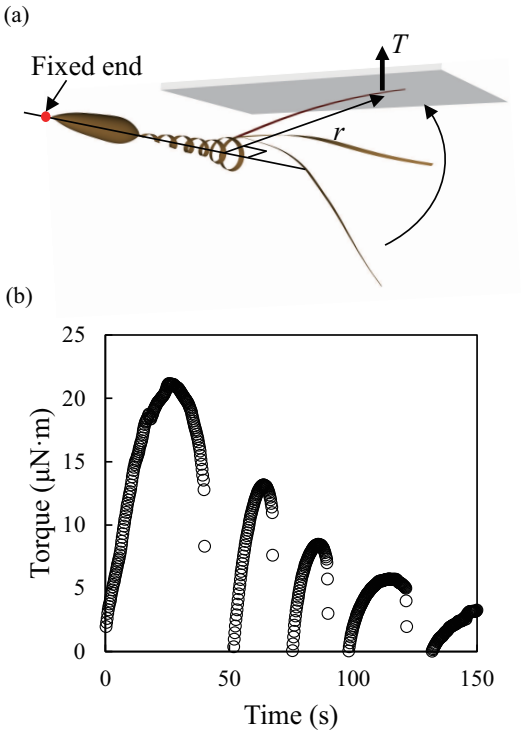

Figure 2.8: (a) Experimental set-up to measure torque induced by rotation of the awn's tail. (b) Measurements of the force exerted on the load cell during rotation of the awn's tail.

head of the seed. We experimentally measured the torque exerted by the end of an awn of *P. carnosum* (Fig. 2.8 (a)) as it rotates with the increase of humidity. Fig. 2.8 (b) shows that the force is measured by the load cell in a cyclical manner because the awn periodically loses contact with the sensor because of rotation. The representative data indicate that the maximum force produced by the awn's rotation is ~ 1 mN, the same order of magnitude as the extensional force. The peaks of the force decrease in magnitude with time, as consistent with the tendency observed in Fig. 2.7 (b), because of the decrease of Young's modulus with increasing water content in the awn's tissue. The length of the tail corresponds to the moment arm, which measures 20 mm, and thus the maximum torque generated by the hygroscopic deformation is on the order of 20 μNm.

We now consider whether the forces generated by the awn are strong enough to enable the seeds to dig into soil. To this end, we measured the forces required for the seeds to dig into soils of different sizes of grains. As model soils, we used glass beads with average diameters of 0.25, 0.83, and 1.40 mm, which represent typical sands of fine, medium, and coarse grains, respectively (Wentworth, 1922). The force exerted by the seed on the soil was measured as a function of the distance the seed moved into the soil. Fig. 2.9 (c) shows that the force (filled symbols) tends to increase almost linearly with the displacement of glass beads of an average diameter of 0.25 mm. As the seed travels 4 mm into the soil, a typical length of the head of the seed as shown in Fig. 2.9 (b), the force increases to ~ 3 mN, a typical value of the maximum extension force of the uncoiling awn. For larger beads (Figs. 2.9 (d) and (e)), the forces periodically peak and drop, supposedly because of the jamming and relaxation of the glass beads that interact with the seed-head of similar transverse diameter as that of the bead. We see that the measured peak forces in the glass beads increase with the size of bead, so that the peak force is ~ 5 and 7 mN for glass beads with an average diameter of 0.83 and 1.40 mm, respectively. Considering that the maximum force arising from the extension of the awn spring typically ¡3

mN, the linear translation of the seed into soils of relatively large grains is likely to be severely blocked by the soil's resistance.

The most remarkable difference between the self-burial behavior of *Erodium* and *Pelargonium* seeds and that of wild wheat is that they rotate, or screw into ground with helically coiled awns. Therefore, we quantify the effects of rotation during digging of the seeds by rotating the soil container while it is being raised. Fig. 2.9 (c)-(e) shows that the resistance of the soil against the penetrating seed is greatly reduced when the seed rotates (empty symbols), so that the force needed to push the seed into the ground is much less than the maximum extension force of the awn spring. These experiments show that the rotation greatly eases the seed's penetration into soil. For beads of average diameters of 0.25, 0.83, and 1.40 mm, rotation reduces the maximum forces experienced by the seed by 75%, 70%, and 73%, respectively. This reduction is sufficient that the extension of the awn spring overcomes the soil's resistance. It is interesting to note that an analogous mechanism is employed by Atlantic razor clams(*Ensis directus*) that burrow into sand via local fluidization caused by the motion of their valves (Winter *et al.*, 2012).

2.6 Conclusions

In this work, we have provided physical accounts of hygroscopically driven botanical movements, which particularly lead to helical coiling and uncoiling of awns of *Erodium* and *Pelargoium* seeds. We suggest that the observed helical rotation of *Pelargonium* awns in response to environmental changes in humidity is caused by the tilted arrangement of the microfibrils in the inner layer of the awn's cell walls, based on the similarity of the awn's structure to that of *E. cicutarium* awns (Abraham & Elbaum, 2013a). We have also presented experimental measurements of the mechanical characteristics of *P. carnosum*'s awns that enable self-burial of the seeds in the soil. The extensional force of the awn can be approximately modeled by the theory of elasticity for a coiled spring. Although the resistance to the seed's

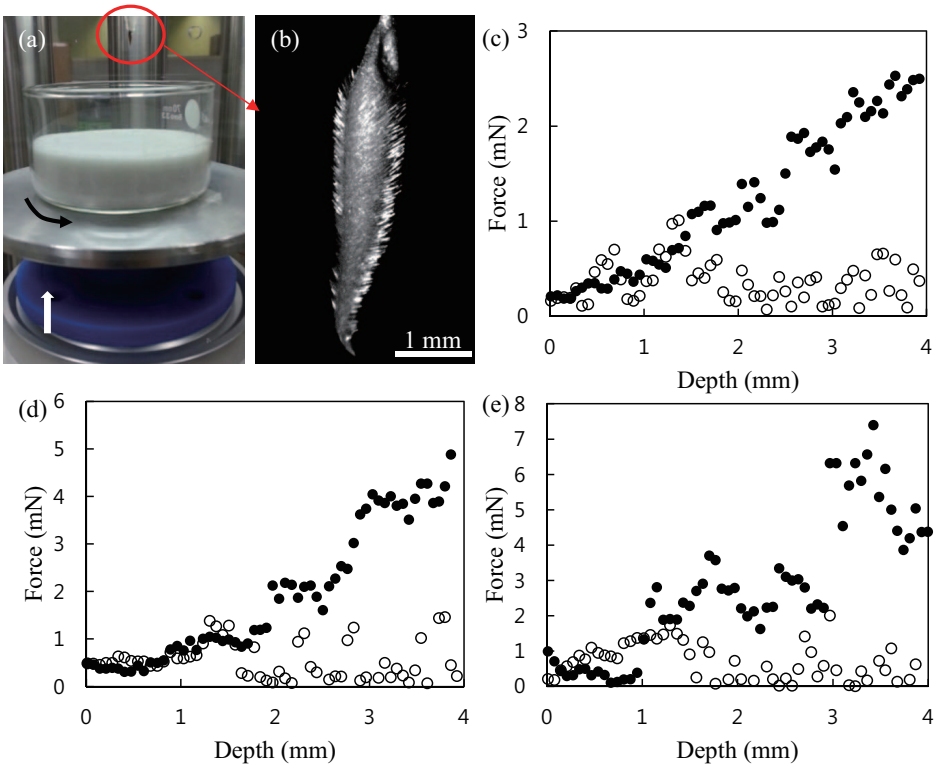

Figure 2.9: (*a*) Experimental measurement of the resistance of soil against penetration of a seed (enclosed in a red circle). (*b*) Optical micrograph of the head of a *Pelargonium carnosum* seed. The lower end touches soil. Measurements of the force exerted by the seed on the glass beads as a function of the distanced the seed moves into the beads with an average diameter of 0.25 (*c*), 0.83 (*d*), and 1.40 mm (*e*). The filled and empty symbols correspond to the forces of the unspinning and spinning seeds, respectively.

head penetrating relatively coarse soils without spinning is larger than the extensional force of the awn spring, the rotation of the seed is shown to greatly ease the digging of the seed into soil. Therefore, we may conclude that the awn's hygroscopic coiling, combined with the axial extension and rotation is critical for the success of this self-burial behavior.

Our quantitative measurements of the awn's force and torque, and the soil's resistance, with and without rotation of the seed, naturally led to the question of the detailed mechanism behind the seed-head's rotation giving rise to such dramatic decrease in the forces needed to advance the seed into the soil. The fact that the seed's head is shaped like a cone must assist in self-burial, but whether the cone's angle has been optimized for such screwing should be answered by further research. The water-driven helical motion of the awns suggests a new actuating mechanism for artificial micro-robots that harness environmental energy associated with changes of humidity in time, or of humidity gradients over space.

Chapter 3

Quasi-static drag force in shallow granular media

3.1 Introduction

Drag force is always bound to a moving object in fluid. In granular media, a moving object also experiences resistance forces. Although there are various attempts to explain granular drag forces with the help of classical fluid mechanics (Chehata *et al.*, 2003; Seguin *et al.*, 2011), it is difficult to explain the granular drag with fluid mechanics due to the complex nature of granular media, which is hardily observed in Newtonian fluids (Forterre & Pouliquen, 2008). Since visco-elastic (Schall & van Hecke, 2010), jamming (Majmudar *et al.*, 2007) and stick-slip (Albert *et al.*, 2000) behaviors are representative characteristics of granular materials, multi-physics should be considered together to understand granular drag.

In fluid mechanics, the drag coefficient C_d is determined by Reynolds number Re, which is a dimensionless number that is defined as the importance of the inertial forces relative to the viscous forces (White, 2006). In a similar approach, the internal friction coefficient μ of granular material is determined by inertial number I which is a dimensionless number that is also defined as the importance of the inertial forces relative to the static friction forces acting on the a moving object (da Cruz *et al.*, 2005; Forterre

& Pouliquen, 2008; MiDi, 2004). At very low inertial number $I < 10^{-3}$ called as quasi-static flow regime, the inertial forces is negligible, so that the rate-independent static friction mainly contributes the granular drag (Brzinski III *et al.*, 2013). Hence, the quasi-static drag scales with the characteristic length of a moving object and the immersed depth (Albert *et al.*, 2000, 2001a, 1999; Hill *et al.*, 2005). In microscopic point of view, quasi-static drag force is described as the force required to break the force chain networks consisting of the contacts of particles in bulk of granular media (Albert *et al.*, 2000, 2001a, 1999).

In this work, we quantitatively measured the granular drag exerted on the vertically penetrating intruder in quasi-static flow regime. With experimental results, we investigated the effects of the intruder shape, the polydisperse grains, and the relative size between the grain and the intruder on the quasi-static drag in shallow granular media.

3.2 Materials and methods

Various size of glass beads with diameters of 0.15-0.25 (fine), 0.25-0.5 (medium), and 0.5-0.75 (coarse) mm were (SiLibeads®, Sigmund Linder GmbH) used as granular media. The density ρ of glass beads is 2.5 g/cm^3, and the angles of repose Θ of fine, medium, and coarse glass beads are $28 \pm 1.8°$, $24 \pm 1.3°$, and $24 \pm 1.2°$, respectively. We measured the vertical forces for cylindrical and conical intruders with a penetration speed $v = 0.2$ mm/s. The radius of the cylindrical intruder R ranges from 1 to 10 mm, and the apex half angle θ of the conical intruder ranges from 10 to 45°. All intruder were made of carbon steel (SMC45C). The vertical motion of the intruder was controlled by a motorized linear stage (M-ILS150CC, Newport). Using a load cell (CBCL, Curiosity Technology), the granular drag experienced by the intruders was measured while we thrusted the intruders into the container with a diameter D of 95 mm and a height H of 50 mm, which is filled with glass beads. Experimental set-up and geometry of the intruder are shown in Fig. 3.1.

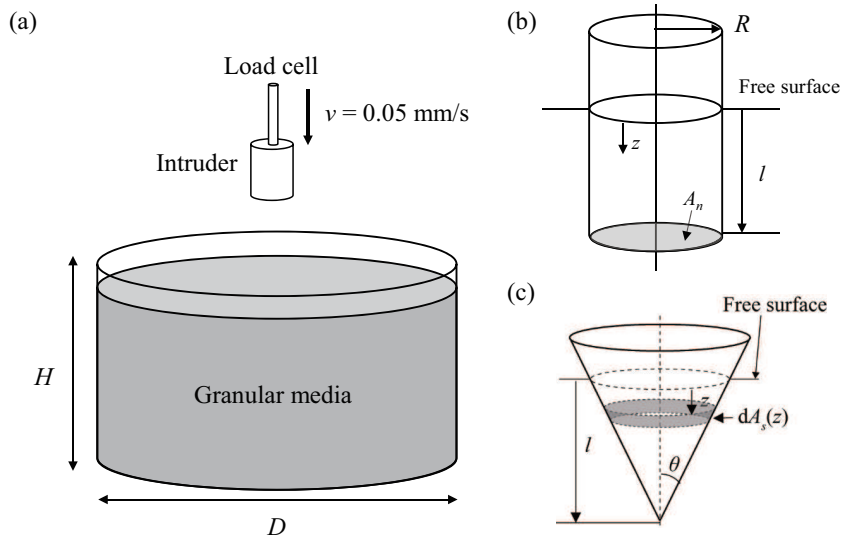

Figure 3.1: (a) Experimental set-up to measure the vertical forces for the intruder. Geometry of the cylindrical intruder (b) and the conical intruder (c).

3.3 Results and discussion

3.3.1 Vertical drag in quasi-static flow regime

An equation of motion of the vertically penetrating intruder within granular media can be described as $ma = F(z) + bv^2$, where ma is the total force acting on the intruder, $F(z)$ is a rate-independent static friction, which is a function of the depth z, and bv^2 is a dynamic friction forces proportional to the square of vertical velocity v^2. The importance of the dynamic friction relative to static friction $F(z)/bv^2$ can be expressed as $A\rho v^2/AP$, where A is the cross-sectional area of the intruder, ρ is the grain density, and P is the hydrostatic pressure. The root square of the ratio of a dynamic friction force to a static friction force yields the dimensionless number $I = v/(P/\rho)^{1/2} = \dot{\gamma}d/(P/\rho)^{1/2}$, where $\dot{\gamma}$ is the shear rate, d is the grain diameter (da Cruz *et al.*, 2005; Forterre & Pouliquen, 2008; MiDi, 2004). In quasi-static flow regime $I < 10^{-3}$, a rate-independent static friction $F(z)$ mainly responsible for granular drag while neglecting the dynamic

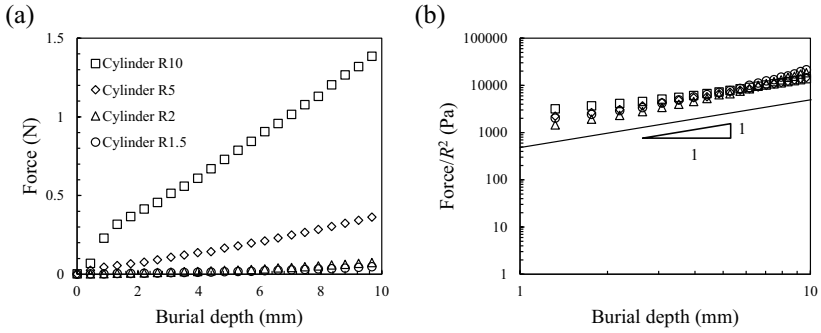

Figure 3.2: (a) The average vertical forces ($n = 5$, where n is the number of experiments) for the cylindrical intruders. The radiuses of the cylindrical intruder R are 1.5 (circle), 2 (triangle), 5 (diamond), and 10 (retangle) mm. Glass beads with diameter of 0.25-0.5 mm are used as granular medium. (b) Drag forces divided by R^2 in log-log representation.

friction bv^2. With knowledge of the static friction depending on the normal force, $\mathrm{d}F(z)$ can be expressed as $\mathrm{d}F(z) \sim \mu P \mathrm{d}A_n \sim \mu\rho \mathrm{gzd}A_n$, where g is the gravitational acceleration and $\mathrm{d}A_n$ is a surface element which the granular hydrostatic pressure normally acts on. The vertical drag force can be estimated by integration of $\mathrm{d}F(z)$ with respect to z from 0 to the burial depth l.

A_n of the cylindrical intruder is independent of the burial depth z, so that $A_n = \pi R^2$, where R is the radius of the cylindrical intruder in Fig. 3.1(b). Therefore, the vertical force acting on the cylindrical intruder is simply expressed as $F \sim \pi\mu\rho g l R^2$ at burial depth l. However, in case of the conical intruder, A_n varies with the burial depth. Consider a conical intruder with an apex half angle θ at the burial depth l in Fig. 3.1(c). The vertical force acting on the differential volume with a thickness of $\mathrm{d}z$ is expressed as $F(z) \sim \mu P \mathrm{d}A_n \sim \mu\rho g z \mathrm{d}A_s \sin\theta$, where $A_s = 2\pi(l - z)(\tan\theta/\cos\theta)\mathrm{d}z$. Integration of $\mathrm{d}F(z)$ with respect to z from 0 to l yields $F \sim (\pi/3)\mu\rho l^3 \tan^2\theta$. Note that the vertical drag force for the cylindrical intruder linearly increases with the burial depth, $F/R^2 \sim l$, and the vertical drag force for the conical shows cubic dependence on the burial depth,

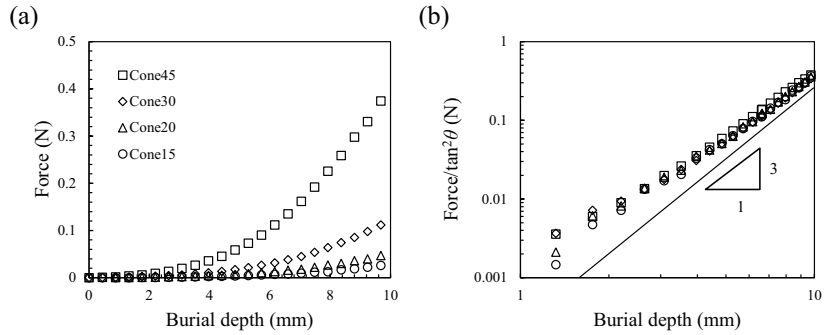

Figure 3.3: (a) The average vertical forces ($n = 5$, where n is the number of experiments) for the conical intruder. The apex half angles of the conical intruder θ are 15 (circle), 20 (triangle), 30 (diamond), and 45 (retangle) mm. Glass beads with diameter of 0.25-0.5 mm are used as granular medium. (b) Drag forces divided by $\tan^2\theta$ in log-log representation.

$F/\tan^2\theta \sim l^3$.

In our experiments, we get $\dot{\gamma} < v/d \sim 0.5$ S^{-1} and $P = \rho g l \sim 0.25$ kPa, where $l \sim 10$ mm, so that $I < 10^{-3}$, indicating a quasi-static flow regime, in which the granular drag mainly depends on the static friction $F(z)$. Experimental results of the vertical drag forces for the cylindrical and conical intruder are shown in Fig. 3.2 and 3.3, respectively. The vertical drag of the cylindrical intruder increases with the burial depth l and the radius of the cylindrical intruder R in Fig. 3.2(a). The drag forces divided by R^2 of the cylindrical intruders collapse in a single curve, which shows a linear dependence on the burial depth l in Fig. 3.2(b). In case of the conical intruder, the drag force increases with the burial depth and the apex half angle θ, as shown in Fig. 3.3(a). The drag forces divided by $\tan^2\theta$ of the conical intruders also collapse in a single curve, which shows a cubic dependence on the burial depth l in Fig. 3.3(b). These indicate that the hydrostatic pressure normally acts on the intruder in quasi-static flow regime. Furthermore, such quasi-static dependence is still valid even in shallow burial depth $l = 10mm$, which is comparable with the intruder size.

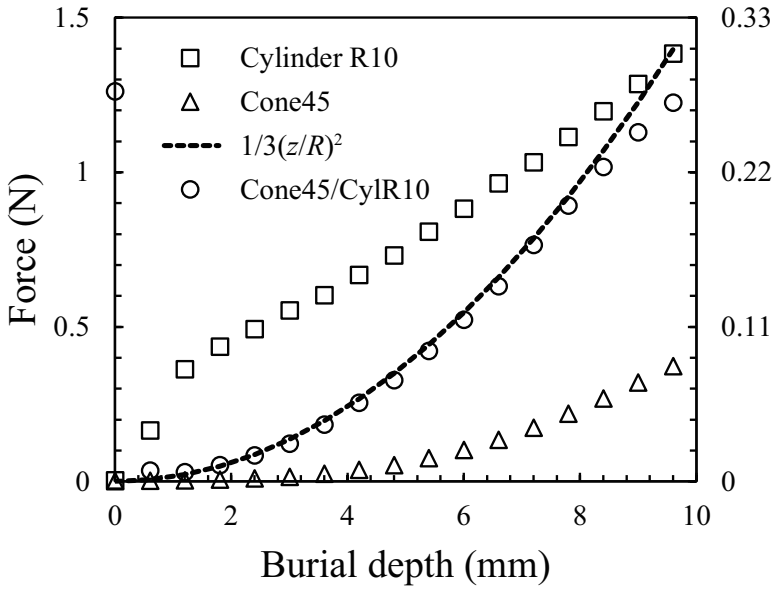

Figure 3.4: Comparison of the drag force of the cylindrical intruder (rectangle) and that of the conical intruder (triangle). The ratio of the drag force of the conical intruder to that of the cylindrical intruder (circle) is in a good agreement with the submerged volume ratio between the conical and cylindrical intruder, $1/3(z/R)^2$ (dotted line).

Next, we investigated the effects of intruder shape on granular drag. In quasi-static flow regime, the granular drag is given by $F \sim \mu\rho g l A_n \sim \mu\rho g V_s$, where $V_s = lA_n$ corresponds to the submerged volume of the intruder within granular media, which is reminiscent of buoyant force upwardly acting on the submerged object in fluid. Therefore, a small submerged volume of the intruder experiences less granular drag. At a specific burial depth l, the conical intruder with the submerged volume of $(1/3)l^3\tan^2\theta$ is smaller than the cylindrical intruder with a radius of $l\tan\theta$ by 1/3. Our experiments show that the ratio of the drag force of the conical intruder to that of the cylindrical intruder is consistent with the ratio of the submerged volume of the conical intruder to that of the cylindrical intruder in Fig. 3.4.

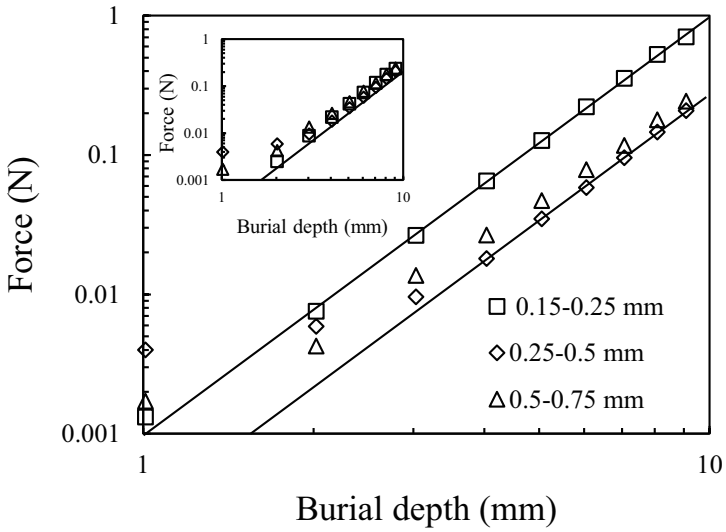

Figure 3.5: The average drag forces ($n = 3$) for the conical intruder with an apex half angle $\theta = 45°$ in three different granular media with diameters of 0.15-0.25 (rectangle), 0.25-0.5 (diamond), and 0.5-0.75 (triangle) mm. Dividing by the relative homogeneity factor $\beta = 3$, the drag forces in granular medium with diameter of 0.15-0.25 mm are consistent with the drag force curves of 0.25-0.5 and 0.5-0.75 mm (inset). Solid lines indicate a cubic dependence on the burial depth.

3.3.2 Effects of polydisperse grains on granular drag

To examine the size effects of grains, we measured the drag force for the conical intruder with an apex half angle $\theta = 45°$ into three different sizes of glass beads media with diameters of 0.15-0.25 (fine), 0.25-0.5 (medium), and 0.5-0.75 (coarse) mm. In Fig. 3.5, the drag force in granular medium with diameter of 0.15-0.25 mm is larger than the others, which are similar with each other, but not change in a cubic dependence on the burial depth. As shown in Fig. 3.6, the granular medium with diameter of 0.15-0.25 mm, whose size distribution is highly polydisperse (see Fig. 3.6(a)), while the granular media with diameters of 0.25-0.5 and 0.5-0.75 mm are relatively monodisperse as shown in Fig. 3.6(b) and (c). With limitation of sieving

method of separating grains according to size, the fine granular medium is likely to contains the non-spherical and irregular grains, and very small grains with diameter of several tens of micrometers. In 2-D plane, the maximum contact number per monodisperse spherical grain has a constant value as 6 in hexagonal close packing even under high stress. However, the contact number in polydisperse granular medium is larger than the minimum 6 and dramtically increases according to the polydispersity of grains under stress. Such increase of the contacts between polysdisperse grains leads a strong jammed state in granular bulk. Therefore, the interlocking between grains forms the strong force chain networks which resist the penetration of the intruder. In same reason, the angle of repose Θ of fine granular medium is larger than the others due to the polydisperse grains (see 3.2 Materials and Methods).

We defined the relative homogeneity factor as $\beta = F_{poly}/F_{mono}$, where F_{poly} is the drag force in polydisperse granular medium and F_{mono} is the drag force in monodisperse granular medium. The relative homogeneity factor of the fine granular medium to the medium and coarse granular medium is calculated as $\beta = F_{fine}/F_{medium} = F_{fine}/F_{coarse} \sim 3$. Dividing by the relative homogeneity factor $\beta = 3$, the drag forces for fine granular medium collapse into the drag force curves for medium and coarse granular media (see inset in Fig. 3.5). When one get the drag force for a intruder in ideally monodisperse granular medium F_{mono}, the relative properties of an unidentified granular medium related with the size distribution, angularity, morphology, and etc. of grains are estimated by the relative homogeneity factor $\beta = F_{unid}/F_{mono}$, where F_{unid} is the drag force in an unidentified granular medium.

3.3.3 Effects of particle size on stick-slip fluctuation

In addition, we also investigated the microscale effects of the grain size on granular drag in quasi-static flow regime. As shown in Fig. 3.7(a), the drag forces fluctuate, and the amplitude of the fluctuation increases with the grain size. While the intruder penetrates into granular media, the force

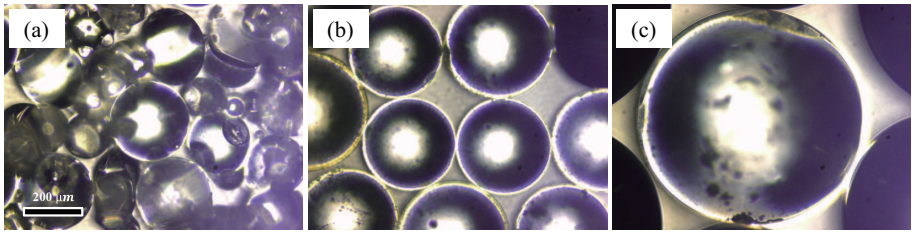

Fine 0.15-0.25 mm Medium 0.25-0.5 mm Coarse 0.5-0.75 mm

Figure 3.6: Optical images of glass beads with diameters of 0.15-0.25(a), 0.25-0.5 (b), and 0.5-0.75 (c) mm. Scale bar is 200 μm.

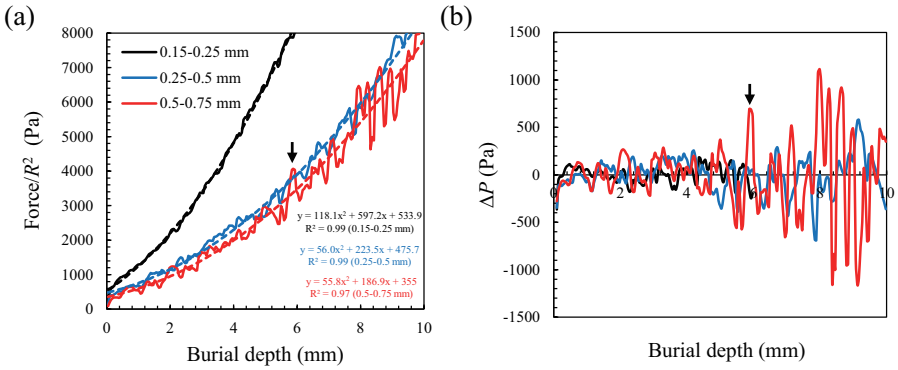

Figure 3.7: (a) The average drag forces (n =5) for the cylindrical intruder with radius of 2 mm in three different granular media with diameters of 0.15-0.25 (black line), 0.25-0.5 (blue) and 0.5-0.75 (red) mm. Sampling time is 5 Hz. Dotted lines are 2nd degree polynomial trend-lines. (b) The difference ΔP between the measured drag force divided by R^2 and the value calculated from the 2nd polynomial curve equation. Black arrows indicate the same data.

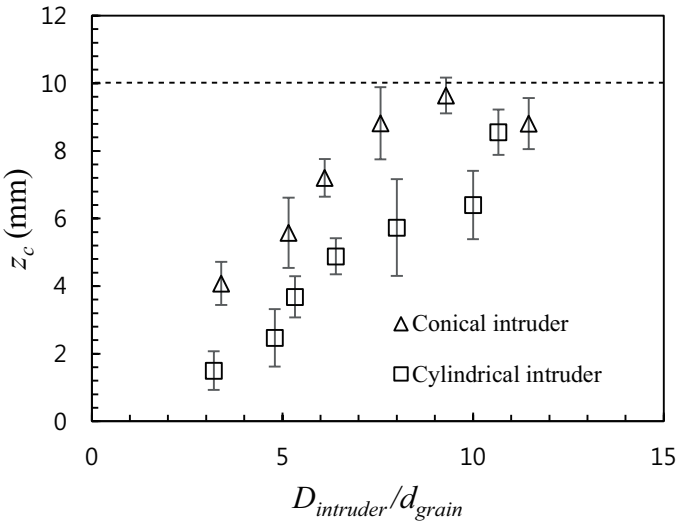

Figure 3.8: The critical stick-slip fluctuation depth z_c for the cylindrical and conical intruders according to the relative size ratio D_{int}/d_{grain}, where D_{int} is the maximum diameter of the intruder and d_{grain} is the average grain diameter. Dotted line indicates maximum burial depth $l = 10$ mm.

chains repeatedly accumulate and relax near the intruder, leading to grain-scale fluctuation called as stick-slip fluctuation. To quantitatively examine the effects of grain size on stick-slip fluctuation, we calculated the difference between the measured drag force divided by R^2 and the value calculated from the 2nd degree polynomial curve equation at a given burial depth as $\Delta P = P_{measure} - P_{trend-line}$ (see Fig. 3.7(b)).

We defined that the stick-slip fluctuation begins at the critical stick-slip fluctuation depth z_c, where $\Delta P > 500$ Pa (see the black arrow in Fig. 3.7(b)). In a similar method, we also defined the critical stick-slip fluctuation depth z_c for the conical intruder, where $\Delta F/\tan^2\theta > 10$ mN. Fig. 3.8 shows the critical stick-slip fluctuation depth z_c for the cylindrical and conical intruders according to the relative size ratio D_{int}/d_{grain}, where D_{int} is the maximum diameter of the intruder and d_{grain} is the average grain diameter. The critical stick-slip fluctuation depth z_c increases with the relative size ratio D_{int}/d, which indicates the number of grains supporting

the penetrating intruder. Furthermore, z_c for the conical intruder is larger than z_c for the cylindrical intruder. These results imply that the grains beneath the conical intruder easily slip out, so that the rearrangement time-scale of grains beneath the conical intruder is shorter than that for the cylindrical intruder due to the inclined plane of the conical intruder. For $D_{int}/d_{grain} > 12$, the stick-slip fluctuation is hardly observed up to the burial depth $l = 10$ mm.

3.4 Conclusion

To investigate various effects on granular drag in quasi-static flow regime, we quantitatively measured the drag forces acting on vertically penetrating intruder in granular medium. We experimentally demonstrated that the quasi-static drag force normally acts on the intruder surface, and depends on the submerged volume of intruder, which is reminiscent of the buoyant force in ordinary fluid. We also showed that the polydispersity of grains greatly increases the granular drag due to the strong interlocking between the grains. Using the relative homogeneity factor β, the relative properties of an unidentified granular medium can be estimated. In addition, the relative ratio of the grain size to the intruder size affects the grain-scale fluctuation, called as stick-slip fluctuation. In addition, our work focused on the drag force within shallow burial depth up to 10 mm. Although the intruder size is comparable with the burial depth, the drag force acts on the intruder in quasi-static manner. Our work can give an explanation of the shape of small-size animals which slowly moving beneath the ground, and provides the detailed parameters to design biomimetic robots working in granular media.

Chapter 4

Reduction of granular drag inspired by self-burrowing rotary seeds

4.1 Introduction

Ingenious mobility strategies have been evolved in animals (Hosoi & Goldman, 2015; Jung, 1987; Li *et al.*, 2013; Maladen *et al.*, 2009; Winter *et al.*, 2012) and plant roots (Bengough & Mullins, 1990; Bengough *et al.*, 1997) in granular environment such as soil, where mobility is significantly reduced by intergranular resistance. Some *Erodium* and *Pelargonium* species, flowering plants belonging to a genus of the family Geraniaceae, produce seeds with an appendage that is used for the seed dispersal and burial (Abraham & Elbaum, 2013a; Abraham *et al.*, 2012; Evangelista *et al.*, 2011; Jung *et al.*, 2014; Stamp, 1984). Fig. 4.1 shows the seed awns of three *Pelargonium* species. Each awn is composed of materials with different hygroscopic expansiveness, and thus responds to a change in humidity (Abraham & Elbaum, 2013a; Abraham *et al.*, 2012). In a humid environment at night time or after a rain fall, a helically coiled awn deforms to a linear configuration, and the deformation can create thrust against the soil when one end of the awn is anchored (Stamp, 1984). Owing to the helical

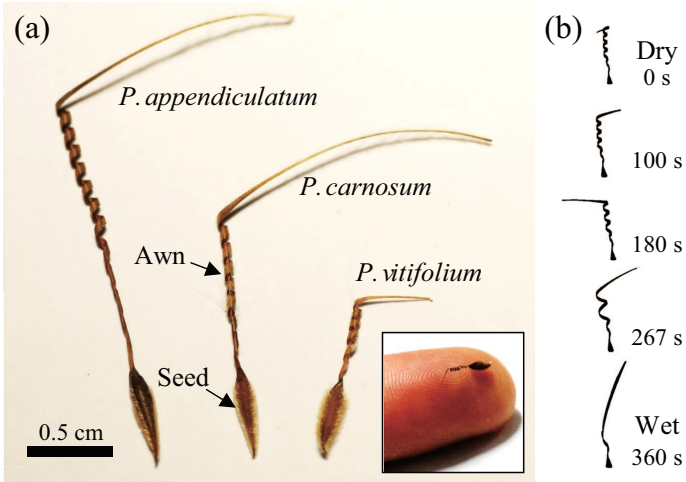

Figure 4.1: Seeds of *Pelargonium* species. (*a*) Three *Pelargonium* species seeds with hygroscopically responsive awns: *P. appendiculatum* (left), *P. carnosum* (middle) and *P. vitifolium* (right). Inset image indicates the size of a seed of *P. vitifolium* in comparison with a human finger. (*b*) The helical awn of *P. carnosum* spontaneously uncoils to a linear configuration in a humid environment.

shape of the awn, the hygroscopic expansion entails a rotary motion during the extension. This locomotory scheme reminds us of a conventional drilling machine or an auger with a rotational intruder, so it is highly probable that the seeds spin themselves to facilitate the digging into soil.

Granular drag on a body in quasi-static motion is mainly associated with the forces for breaking intergranular contacts in a jammed granular medium (Albert *et al.*, 2000, 2001a, 1999). The jamming and relaxation of grains cause stick-slip (Albert *et al.*, 2000), pressure-screening (Bertho *et al.*, 2003), and visco-elastic behaviors (Schall & van Hecke, 2010). When a rod rotates bout an axis passing through the center, perpendicular to the plane of the rod, it disturbs the arrangement of the jammed grains, so that the rotational torque dramatically decreases after half a turn at a given depth (Guillard *et al.*, 2013). Although a few mathematical models for granular drags are available under limited conditions (Brzinski III & Durian, 2010; Guillard *et al.*, 2013; Soller & Koehler, 2006), understand-

ing of the drag force for a vertically penetrating rotary intruder remains incomplete due to complicated intergranular mechanics.

Motivated by the self-burrowing rotary seeds, we here elucidate the reduction of granular drag by rotation for a vertically penetrating intruder. We found that the vertical drag against a rotating intruder decreases with its rotation speed. Noting that the relative motions of the grains in contact with the intruder induce the collapse of the force chains in the granular bulk, we developed a model for the drag reduction by rotation in terms of the slip velocity of the grains, which successfully explains the drag reduction of the rotating intruders including self-burrowing rotary seeds.

4.2 Results and discussion

4.2.1 Vertical granular drag in quasi-static flow regime

We start with quantifying the drag reduction experienced by the biological examples through their rotation. We measured the granular resistance of seeds of three *Pelargonium* species during their vertical penetration in a granular medium. Fig. 4.2(a) illustrates the experimental setup to measure the drag forces. The seeds were forced into soil with a speed $v = 0.2$ mm/s in the container filled with glass beads of a diameter ranging from 250 to 500 μm, and the drag forces were measured by a load cell. As shown in Fig. 4.2(b), the drag force depends on the shape and size of the seed head, but increases with the burial depth for all cases. To test the drag reduction by spinning, we rotated the container of the glass beads around the axis of the seed at a rate of 7 rpm, the maximum rotation speed observed for a wet awn, as thrusting the seed at $v = 0.2$ mm/s. The granular resistance significantly decreased for all seeds by up to 75% in Fig. 4.2(b), demonstrating that a self-burrowing seed can indeed reduce the granular drag with its rotational motion.

We develop a mathematical model to understand this marked reduction of granular drag. The importance of the dynamic friction relative to static friction depends on the inertial number $I = \dot{\gamma}d/(P/\rho)^{1/2}$, where $\dot{\gamma}$ is the

shear rate, d is the grain diameter, P is the hydrostatic pressure, and ρ is the density of grain (da Cruz *et al.*, 2005; Forterre & Pouliquen, 2008; MiDi, 2004). n our experiment, the maximum rotational speed ω is 10 rpm, so that the tangential velocities of the rotating intruder $v_r < \omega r_{eff} \sim 1$ mm/s where the radius of rotation r_{eff} is on the order the seed thickness of 1 mm, and the shear rate $\dot{\gamma} < (v^2 + v_r^2)^{1/2} \sim 3$ s^{-1}. In addition, $P = \rho g l \sim 0.25$ kPa, where g is the gravitational acceleration, $l = 10$ mm is the burial depth, and $\rho = 2.5$ g/cm^3. Accordingly, we calculate that $I < 3 \times 10^{-3}$, indicating a quasi-static flow regime (MiDi, 2004),in which the granular resistance depends exclusively on the static friction. Therefore, the normal force by static pressure on the intruder surface is mainly responsible for the drag (Brzinski III *et al.*, 2013).

Consider a conical intruder with an apex at a distance l below the free surface, as shown in Fig. 4.2(a). We express the vertical force acting on the differential volume with a thickness of dz at the depth z from the free surface as $\mathrm{d}F(z) \sim \mu P \mathrm{d}A_s \sin\theta$, where μ is the internal friction coefficient, θ is the apex half angle of the conical intruder, and dA_s is the surface area of the intruder element. With $\mathrm{d}A_s = 2\pi(l - z)(\tan\theta/\cos\theta)\mathrm{d}z$ and $P = \rho g z$, integration of d$F(z)$ with respect to z from 0 to l yields $F \sim (\pi/3)\mu\rho g l^3 \tan^2\theta$. If we define the effective resisting area $A_e = (\pi/3)l^2 \tan^2\theta$, the drag force can be simply expressed as $F \sim \mu P_t A_e$, where $P_t = \rho g l$ is the hydrostatic pressure at the intruder tip. Therefore, the granular drag increases with the apex half angle and burial depth. We experimentally examined the drag on the conical intruders with the various apex half angles θ of 20°, 30°, and 45° to the burial depth of about three seed lengths. Fig. 4.2(c) presents the drag forces on the intruders, and the data points collapse onto a line predicted by the model, $F/\tan^2\theta \sim l^3$.

We briefly discuss the advantage of the conical shapes of *Pelargonium* seeds for self-burial behavior. In quasi-static flow regime, the granular drag is given by $F \sim \mu\rho g l A_e$, where lA_e corresponds to the effective submerged volume of the intruder in granular media. Therefore, a small effective submerged volume of the intruder is advantageous for reducing the granular

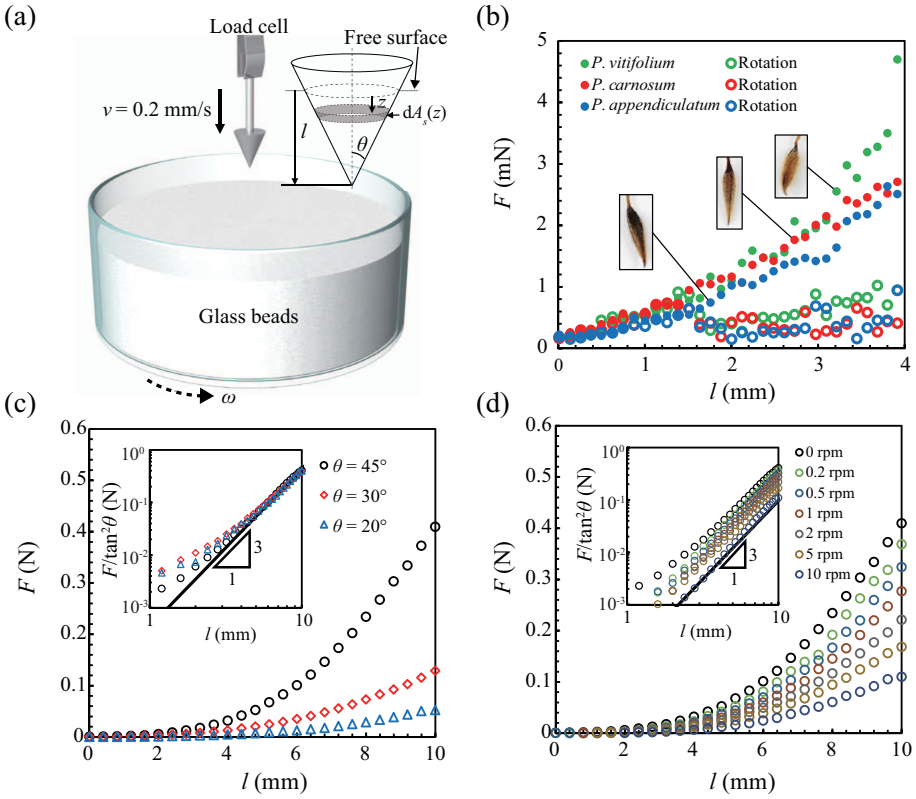

Figure 4.2: Measurement of drag force. (a) Schematic illustration of experimental setup to measure the drag force for the vertical penetration of the seed or intruder. The container with a diameter of 95 mm and a height of 50 mm is filled with glass beads mimicking soils. While thrusting the seed or intruder into the glass beads with a constant velocity, the force is measured by a load cell. (b) Dependence of the average drag force ($n = 5$, where n is the number of experiments) on the burial depth. For rotation test, the container rotates with a speed of 7 rpm at a burial depth of 1.5 mm. Filled and empty symbols correspond to the drag force without rotation and with rotation, respectively. (c) Drag forces F for the conical intruders with the various apex half angles, $\theta = 20°$, $30°$, and $45°$. Inset shows that $F/\tan^2\theta$ is proportional to l^3. (d) Granular drag for a rotating intruder with $\theta = 45°$. The granular drag decreases with the angular velocity. Inset shows that rotation does not change the cubic dependence. All measurement points for the conical intruders indicate average values ($n = 3$).

drag in self-burrowing. For instance, a seed with a conical shape with an effective submerged volume of $(\pi/3)l^3 \tan^2\theta$ can reduce the drag force by 1/3 compared with a seed with a cylindrical shape with a radius of $l \tan\theta$ for a given burial depth of l.

4.2.2 Reduction of granular drag by rotation

We measured the granular drag for the intruder with $\theta = 45°$ in a container rotating with a speed ranging from 0.2 to 10 rpm. In Fig. 4.2(d), the drag force is compared with that for an intruder without rotation. The results indicate that the drag force decreases with the angular velocity, and the reduction reaches approximately 75% for the highest rotation speed of 10 rpm in our experiments. At this rotational speed, we measured the torque to rotate the intruder $\tau = 9 \times 10^{-5}$ N·m at a burial depth of 10 mm, so that the shear force by the granular medium scales $F_{shear} \sim \tau/r_{eff} \sim 18 \times 10^{-3}$ N, where the radius of rotation $r_{eff} = 5$ mm was estimated as the half of the base radius of the submerged intruder. Accordingly, we calculate $F_{shear}/F_d = 0.045$, where the vertical drag force F_d for the equivalent condition is approximately 0.4 N (see Fig.4.2 (c)), so that the shear force is insignificant compared with the vertical force. We also found that the rotation of the intruder reduces only the magnitude of the drag without change in the cubic dependence on the burial depth l, implying that the normal static force is still responsible for the granular drag for the rotating intruder. This suggests that the intruder rotation reduces the effective resisting area A_e on which the granular hydrostatic pressure acts.

To aid understanding of the drag reduction by rotation, we present the schematic of the grains beneath the bottom of a rotating intruder in Fig. 4.3. A penetrating intruder encounters force chains that resist its motion. Force chains are a network of intergranular contacts in the bulk medium, and so granular pressure acts on the intruder surface along the force chains (Albert *et al.*, 2000, 2001a, 1999). When an intruder rotates, the rotational motion yields additional intergranular motions, which facilitate to break the force chains (Bocquet *et al.*, 2009; Desmond & Weeks, 2015; Kabla &

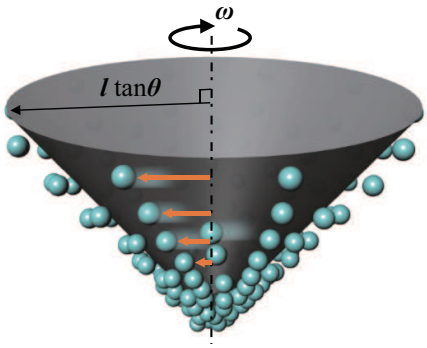

Figure 4.3: Schematic illustration of the motion of grains underneath the intruder. Grains in contact with the intruder surface are in motion owing to the friction. These granular motions promote the intergranular motions in the bulk, which increases the possibility of collapse of the force chains.

Debrégeas, 2003; Reddy *et al.*, 2011), thereby reducing the vertical drag forces. These granular motions promote the intergranular motions in the bulk, which increases the possibility of collapse of the force chains. The local surface speed induced by rotation increases with the radial distance from the intruder centerline, so the grains easily slip in the outer region. In contrast, the force chains are robust in the inner region where the surface speed is relatively low.

4.2.3 Relative slip motion of grains induced by rotation

To quantify the drag reduction by slip motions between the intruder and grains, we experimentally examine the drag reduction ratio with respect to the slip velocity. As shown in Fig. 4.4(a), we measured the vertical drag force of the cylindrical intruder with a radius of 10 mm in a container filled with glass beads while the container translates in the direction orthogonal to that of penetrating. It is observed that the drag decreases with the slip velocity, v_s. Furthermore, we see that the drag reduction ratio depends critically on the relative slip velocity $u = v_s/v$ in the quasi-static flow regime (see Fig. 4.4(a)).

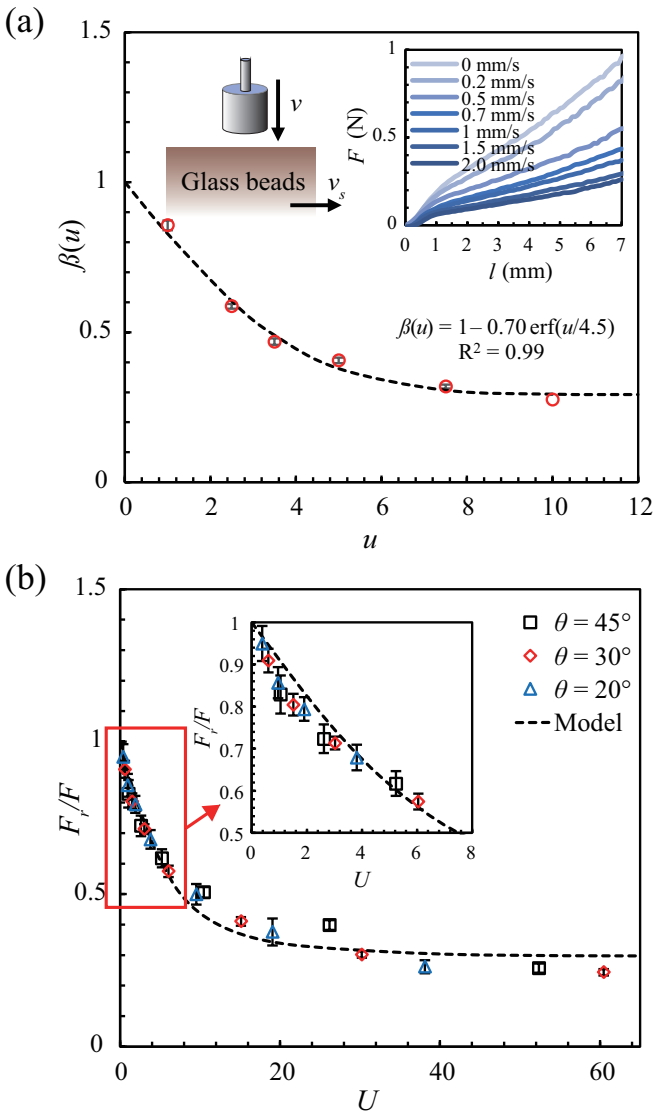

Figure 4.4: Drag reduction by rotational motions. (a) Relative drag force for the cylindrical intruder with a slip to that with $u = 0$. The horizontal velocity v_s of glass beads ranges from 0.2 to 2.0 mm/s while the penetrating velocity v is 0.2 mm/s. The dashed line indicates our empirical model, $\beta(u) = 1 - 0.70\mathrm{erf}(u/4.5)$. In the inset, the granular drag decreases with v_s (n = 3). (b) Dependence of the drag reduction ratio F_r/F on $U = \omega l \tan\theta/v$. The dashed line indicates the model prediction of F_r/F. Inset shows a plot for the range of $0 < U < 8$.

We now seek a correlation for $\beta(u)$, the relative drag force for the intruder with slip to that without slip ($u = 0$). We note that granular medium around a moving object exhibits the visco-elastic characteristic, a reminiscent of a Bingham fluid (**?**). The velocity profiles of shearing grains in various Couette flow systems have been successfully modeled using exponentially decaying functions (Corwin *et al.*, 2005; Fenistein *et al.*, 2004; Mueth *et al.*, 2000). Since the collapse of the force chains is strongly affected by the local slip velocity, we give $\beta(u)$ in the form of the error function, $\beta(u) = 1 - 0.7\mathrm{erf}(u/4.5)$, which shows good agreement with our measurements (Fig. 4.4(a)). This correlation enables us to estimate the local granular drag for a rotating intruder as $\mathrm{d}F_r \sim 2\pi\rho g(l-z)z\tan^2\theta\beta(u)\mathrm{d}z$. The relative slip velocity is given by $u = r\omega/v = (l-z)\tan\theta\omega/v$, where r is the radius of the immersed conical intruder at the depth z below the free surface, and ω is the angular velocity. Numerically integrating $\mathrm{d}F_r$ with respect to z from 0 to l yields granular drag F_r for a rotating intruder at a specific angular velocity.

We define the rotational drag ratio F_r/F as the ratio of the drag for a rotating intruder to that with non-rotating intruder ($\omega = 0$). Fig. 4.4(b) shows the dependence of the ratio on $U = \omega l\tan\theta/v$, where $\omega l\tan\theta$ corresponds to the maximum slip velocity on the contact line between the intruder and grains at the free surface. For various intruders, the reduction ratio rapidly decreases for low U, but saturates as U increases further, which is in agreement with our model prediction. As the relative slip velocity increases, the measured ratio becomes slightly lower than our model because the flow experiences the transition from the quasi-static to dense flow regime where granular medium is more easily fluidized.

4.3 Summary

In summary, we have measured the granular drag against a vertically penetrating intruder with rotation, and found that the drag reduction of a rotating intruder is critically determined by the relative slip velocity.

We have formulated an empirical correlation for the drag reduction by the slip motion, leading to a novel model for the drag of a rotating intruder. This model successfully describes our experimental measurements. Our work rationalizes the drag reduction of the self-burrowing seeds by rotation, which must be advantageous for the survival of the seeds before and during germination. Our study illuminates the functionality and beauty of natural design, as well as provides new insights into the design of self-sustainable drilling robots for military and environmental applications and underground exploration in space (Pandolfi & Izzo, 2013). Visualization of the granular pressure distribution (Corwin *et al.*, 2005; Mueth *et al.*, 1998) and the granular motion (Mueth *et al.*, 2000; Sakaie *et al.*, 2008) beneath the vertically penetrating rotary intruder would further our understanding of drag reduction from a microscopic point of view.

Chapter 5

Effects of rotation on granular jamming: force-dependent electrical resistance in granular medium

5.1 Introduction

Phase of granular systems is determined by the intergranular contacts, which is generally caused by an external load or geometry of a channel where grains can flow (Biroli, 2007; Brown & Jaeger, 2009; Liu & Nagel, 1998; Majmudar *et al.*, 2007; To *et al.*, 2001; Trappe *et al.*, 2001). Above the critical packing fraction of grains, granular system is almost motionless like solid phase, which is called as jammed state. Due to the complex intergranular mechanics, analysis of granular jamming is not complete and limited to observations and visualizations of the formation of the force chains and resulting force distribution in granular media (Clark *et al.*, 2015; Corwin *et al.*, 2005; Majmudar *et al.*, 2007; Mueth *et al.*, 1998, 2000; Yu & Behringer, 2005; Zuriguel & Mullin, 2008). However, they are confined to

2-dimensional observation due to the limitation of opaque grain and complicated optics. In addition, discrete elements methods (DEM) is intensively conducted to visualize the granular jamming process (Muthuswamy & Tordesillas, 2006; Ostojic *et al.*, 2006; Peters *et al.*, 2005; Tordesillas *et al.*, 2014).

In this work, we suggest a simple method to estimate jamming degree by measuring the electrical resistance of granular medium consisting the electrically conductive particles. We note that the force chain, which is a intergranular connection forced by contacts between neighboring grains, plays a role as an electric current path in electrically conductive particles medium (Nawroj *et al.*, 2013; Swensen & Dollar, 2012). As compressing granular medium, the density of the force chains increases, so that the electrical resistance of granular medium decreases. To validate this method, we investigated the relaxation of granular jamming by rotation via measurement of the electrical resistance, which effectively shows an internal jamming process in granular media. Regardless of the geometry of the intruder and container filled with grain, the proposed method can gives collective internal properties of granular media. Our work will be expected to advance granular mechanics related with jamming and relaxation, which are the most important phenomena in granular materials.

5.2 Materials and methods

5.2.1 The measurements of the granular drag in glass beads

To measure the drag reduction by rotation, we used glass beads (SiLibeads®, Sigmund Linder GmbH), whose diameter rages from 250 to 500 μm, as granular medium. Using load cell (CBCL, curiosity technology), we measured the vertical resistive forces for the intruders, while thrusting the intruders into granular medium with rotation and without rotation. In case of rotational motion, we rotated the container filled with glass beads. The vertical and angular motion of an intruder were controlled by a motorized linear stage (ML-ILS150CC, Newprot) and a motorized rotary stage (M-660

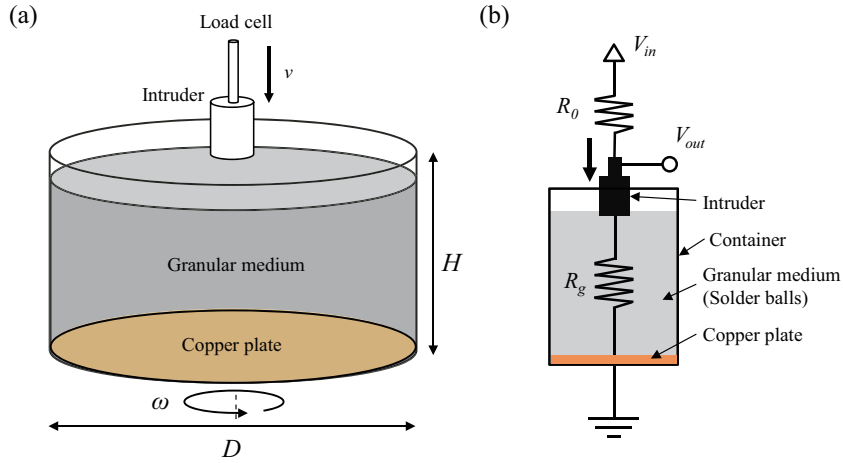

Figure 5.1: (a) Experimental set-up to measure the vertical drag force with rotation and without rotation. The diameter D and height H of the container is 95 mm and 50 mm, respectively. (b) Electrical resistance measurement circuit.

rotation stage, Physik Instrumente (PI)), respectively. The trust speed v was kept at 0.2 mm/s, and the rotational speed was controlled between 0.2 to 5 rpm. The cylindrical intruder were made of carbon steel (SMC45C), and the radiuses of the cylindrical intruders R are 1.5, 2, 5, and 10 mm. Schematic illustration of an experimental set-up is shown in Fig. 5.1(a).

5.2.2 The measurements of the granular drag in solder balls

Using the same experimental set-up, we also measured the granular drag in solder balls. We used various size of electrically conductive solder balls (MK Electron Co., Ltd.) as granular medium, which is highly monodiseperse particles shown as in Fig. 5.2. Using a optical microscope, we measured the diameters of the solder balls (200 EA), as shown in Fig. 5.3. The properties of solder ball are summarized in Table. 5.1. In addition, the conical intruders with an apex half angle of $\theta = 45°$ was used. The trust speed v was kept at 0.05 mm/s, and the rotational speed was controlled between 0.2 to 5 rpm.

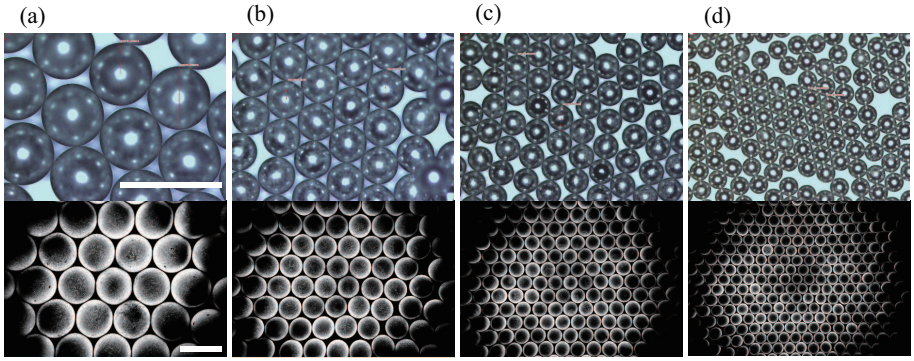

Figure 5.2: Optical images and Scanning Electron Microscope (SEM) images of solder balls with diameters of 500 ± 25 (a), 300 ± 10 (b), 200 ± 3 (c), and 150 ± 3 (d) μm. Scale bar is 500 μm.

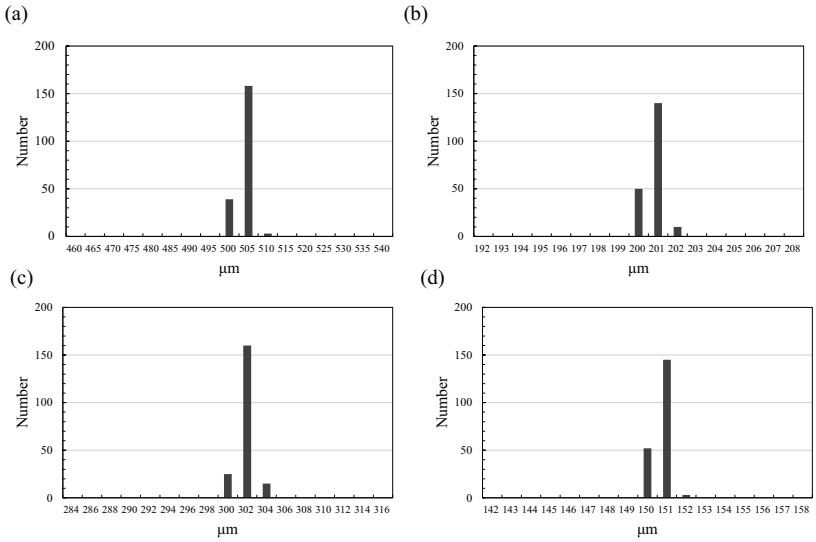

Figure 5.3: Diameter distribution of 500 ± 25 (a), 300 ± 10 (b), 200 ± 3 (c), and 150 ± 3 (d) μm.

Item	Property
Solidus point [°C]	217
Diameter [μm]	150 ± 3, 200 ± 3, 300 ± 10, 500 ± 25
Density [g/cm^3]	7.35
Vickers hardness [HV]	15.6
Tensile strength [MPa]	35
Young's modulus [GPa]	34
Electrical Resistivity [$\mu\Omega$·cm]	14
Composition	Sn-1.2Ag-0.5Cu-0.05Ni

Table 5.1: Properties of solder balls used as granular media.

5.2.3 The measurements of the electrical resistance of granular medium

To measure the electrical resistance of the granular medium consisting of solder balls, we located a copper plate, which is connected with ground, at the bottom of the container filled with solder balls. Using a simple electrical resistance measurement circuit (see Fig. 5.1(b)), we measured the electrical resistance of the granular medium while thrusting the intruder with rotation and without rotation. With $V_{\rm in} = 5$ V and an adjustable resistance $R_0 = 10^5$ Ω, we read $V_{\rm out}$, so that the electrical resistance of granular medium R_g was calculated as $R_g = R_0 \times V_{\rm out}/(V_{\rm in} - V_{\rm out})$.

5.3 Results and discussion

5.3.1 Reduction of granular drag by rotation

The importance of the dynamic friction relative to static friction depends on the inertial number $I = \dot{\gamma} d/(P/\rho)^{1/2}$, where $\dot{\gamma}$ is the shear rate, d is the diameter of grain, P is the hydrostatic pressure, and ρ is the density of solder ball (da Cruz *et al.*, 2005; Forterre & Pouliquen, 2008; MiDi, 2004). With $P = \rho g l$, where g is the gravitational acceleration and l mm is the burial depth, the inertial number I can be simplified as $I = \dot{\gamma}(d/\eta g)^{1/2}$,

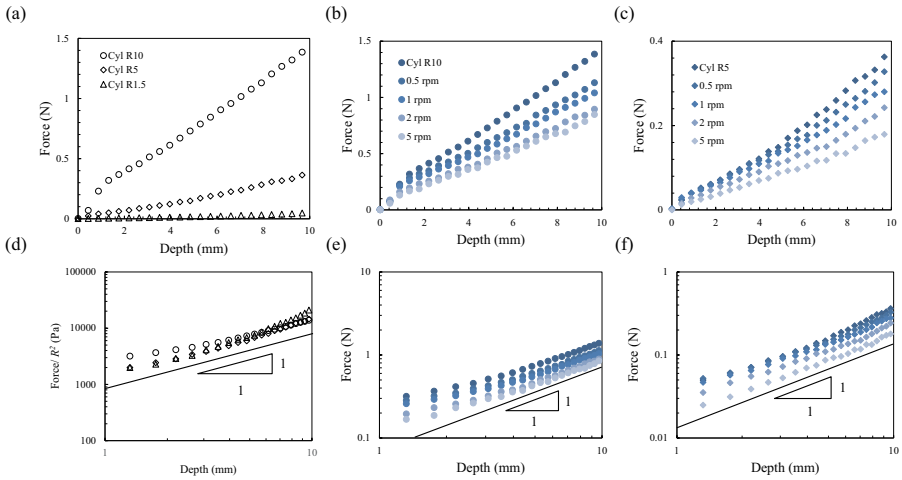

Figure 5.4: (a) The average vertical forces ($n = 5$, where n is the number of experiments) for the cylindrical intruders. The radiuses of the cylindrical intruder R are 1.5 (triangle), 5 (diamond), and 10 (circle) mm. Granular drag for the rotating cylindrical intruders with $R = 10$ mm (b) and $R = 10$ mm (c). The figures of (d), (e), and (f) show the linear dependence on the burial depth for the results of (a), (b), and (c), respectively.

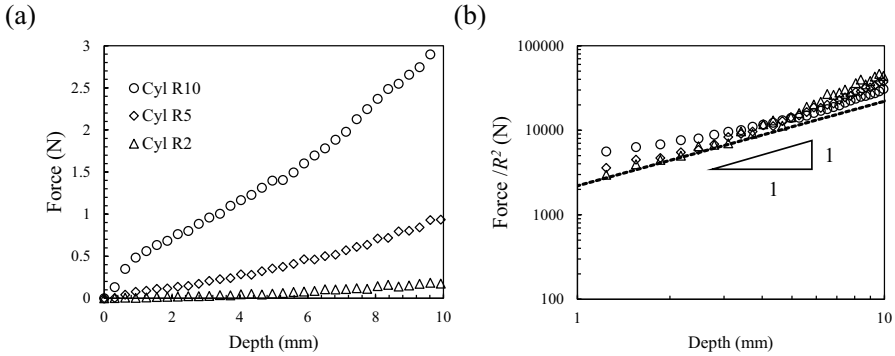

Figure 5.5: (a) The average vertical forces ($n = 3$) for the cylindrical intruders in solder balls. The radiuses of the cylindrical intruder R are 2 (triangle), 5 (diamond), and 10 (circle) mm. (b) The linear dependence on burial depth for all intruders.

where $\eta = l/d$. In our experiment, the thrust speed v is kept as 0.2 mm/s, so that shear rate $\dot{\gamma} = v/d < 0.5$ s^{-1} , where the average diameter of glass beads d is 375 μm. In addition, the burial depth l is 10 mm, so that $I \sim 0.6 \times 10^{-3} < 10^{-3}$, indicating a quasi-static flow regime (da Cruz *et al.*, 2005; Forterre & Pouliquen, 2008; MiDi, 2004),in which the granular resistance depends exclusively on the static friction. Therefore, the normal force by static pressure on the intruder surface is mainly responsible for the drag (Brzinski III *et al.*, 2013).

We also estimated the inertial number I for the rotational case. In our experiments, the maximum rotational speed is 5 rpm, indicating the angular velocity $\omega \sim 0.5$, so that the tangential velocity of the rotating intruder $v_r \sim \omega r \sim 5$ mm/s where the radius of rotation $r = 10$ mm is taken to be the maximum radius of the intruder, and the shear rate $\dot{\gamma} < (v^2 + v_r^2)^{1/2}/d \sim v_r/d \sim 13$ s^{-1} ($v/v_r \ll 1$), where d is 375 μm. On the ground of the shear rate, the inertial number is calculated as $I < 1.6 \times 10^{-2}$, indicating the quasi-static flow regime in rotational case where the internal friction coefficient does not vary with the rotational speed (MiDi, 2004).

In quasi-static flow regime, granular drag acting on the cylindrical intruder is estimated as $F \sim \mu P A_n \sim \mu \rho g l \pi R^2$, where μ is the internal

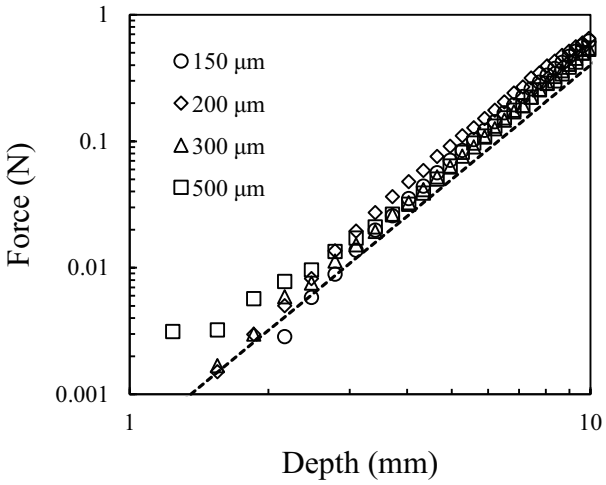

Figure 5.6: The average vertical forces ($n = 3$) for the conical intruders with an apex half angle of $\theta = 45°$ in various solder balls media. Dotted line indicate the cubic dependence on the burial depth.

friction coefficient and $A_n = \pi R^2$ is the normal surface area of the cylindrical intruder. As shown in Fig. 5.4(a), the vertical force increases with the radius R of the cylindrical intruder and burial depth l. In Fig. 5.4(d), F/R^2 for all cylindrical intruders collapse into one curve, indicating that the granular drag force acts on the normal surface A_n. We also measured the vertical drag force acting on the cylindrical intruder with $R = 10$ mm (Fig. 5.4(b)) and $R = 5$ mm (Fig. 5.4(c)) in the container rotating with a speed ranging from 0.5 to 5 rpm. Although the vertical drag force decreases with rotational speed, the linear dependence on the burial depth l is not changed in Fig. 5.4(e) and (f), implying that normal static force is still responsible for the granular drag for the rotating intruder. The rotation of intruder promotes additional intergranular motions, which alter or relax the force chain network near intruder, so that the rotational motion reduce the normal surface area A_n where the granular hydrostatic pressure acts.

5.3.2 Granular drag in solder balls

To investigate jamming in granular media by electrical resistance, we used electrically conductive solder balls as granular medium. First, we experimentally examined the granular drag in solder balls. We measured the vertical drag forces while thrusting an intruder in solder ball medium with a speed v of 0.05 mm/s, indicating the quasi-static flow regime, $I < 10^{-3}$. The vertical drag force also increases with the radius of the cylindrical intruder and the burial depth (see Fig. 5.5(a)), and shows the linear dependence on the burial depth in solder balls medium (see Fig. 5.5(b)).

To investigate the effect of the grain size on the granular drag, we used various size of solder balls with diameter ranging from 150 to 500 μm. As shown in Fig. 5.6, the grain size does not effect the vertical drag forces. Regardless of the grain size, perfectly monodisperse particles have a constant contact number $N = 6$ in 2-D hexagonal close packing (hcp). In case of $d/R \ll 1$ where d and R are the grain size and the intruder size, respectively, the granular drag force acting on the intruder does not vary with the size of monodisperse grains. Furthermore, the vertical drag for the conical intruder is scaled as $F/\tan^2\theta \sim l^3$ in quasi-static flow regime (see Chapter 3.3).

5.3.3 Electrical resistance of granular medium

Next, we measured the electrical resistance of granular medium consisting of electrically conductive solder balls with diameter of 500 μm, while we trusted a cylindrical intruder with a radius of 10 mm in solder balls medium. To make an electrical connection, we placed the copper plate to the bottom of the container filled with solder balls (see Fig. 5.1). As shown Fig. 5.7(a), the vertical force increases with time, which corresponds to the burial depth. On the other hand, the electrical resistance decreases with time. To understand such decreasing of the electrical resistance of solder balls medium during penetration of the intruder, the mechanism of force chain formation should be considered. The force chain is a granular connection consisting of

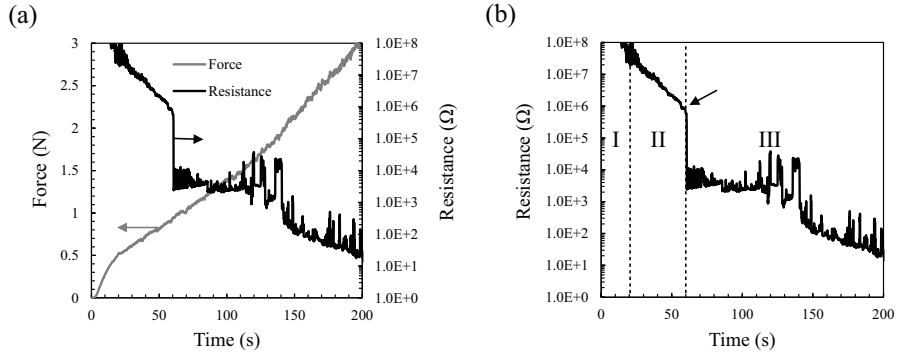

Figure 5.7: (a) The vertical force and electrical resistance for the cylindrical intruder with a radius of 5 mm while trusting the intruder with a speed of 0.05 mm/s in solder balls medium. The time of 200 s equals to the burial depth l = 10 mm. (b) The electrical resistance behavior can be divided by three regions: no-contact (I), plastic deformation (II), and elastic deformation regions (III). The black arrow indicates the sharp drop of the electrical resistance.

the contacts between neighboring grains. As increasing the applied stress, the number of contact and the contact force between neighboring grains increase. Increasing of the length and number of the force chain leads increasing of the bulk density of the granular medium. Above a critical bulk density, granular medium has the strongly inter-locked granular networks and acts as solid phase: granular jamming. In quasi-static flow regime, the granular hydrostatic pressure, which is mainly responsible for the granular drag, acts on the intruder along the force chain. Therefore, force chains resist the penetration of the intruder, so that the drag force acting on the intruder increases with the burial depth. When a granular medium consists of electrically conductive particles, the electrical current can flow along the force chain network between the intruder and the copper plate. Therefore, the electrical resistance of the granular medium decreases with the burial depth during penetration of the intruder.

With this intuitive physical consideration, the measurement of the electrical resistance of granular medium indicates the formation of the force

chain and jammed state in granular medium under stress. The decreasing behavior of the electrical resistance shows three distinct regions: no-contact (I), elastic deformation (II), and plastic deformation regions (III) in Fig. 5.7(b). In no-contact region (I), the formation of the force chains connected with the bottom surface of the intruder is initiated, but not yet connected with the copper plate at the bottom of the container. When the force chains begin to connect with the copper plate, the electrical current can flow along with the force chains, so that the electrical resistance decreases with the burial depth, and has a rapid slope in elastic deformation region (II), where the granular medium shows a large deformation by the penetration of the intruder at shallow burial depth. After that region, the electrical resistance sharply falls down at 60 s (see the black arrow in Fig. 5.7(b)). At this point, the force chains, which are initiated from the bottom surface of the intruder, begin to meet the pre-existing force chains due to the hydrostatic pressure at the bottom of the container. Therefore, the number of the current path from the intruder to the copper plate abruptly becomes large. Then, the electrical resistance is reduced with a relatively slow slope in elastic deformation region (III), where the strong force chains hold granular medium like solid.

We also measured the electrical resistances for various intruders as shown in Fig. 5.8. All curves for various intruders show a similar behavior and also have three distinct regions: (I), (II), and (III) regions. However, the curve shifts to left side as decreasing the intruder size. The drag force increases with the intruder size, indicating that the number of force chain generated by penetration of the intruder also increases with the intruder size.

5.3.4 Effects of rotation on electrical resistance of granular medium

To elucidate the effects of rotation on granular drag, we measured the electrical resistance of solder balls medium. We rotated the container filled with solder balls with diameter of 500 μm around the central axis of the

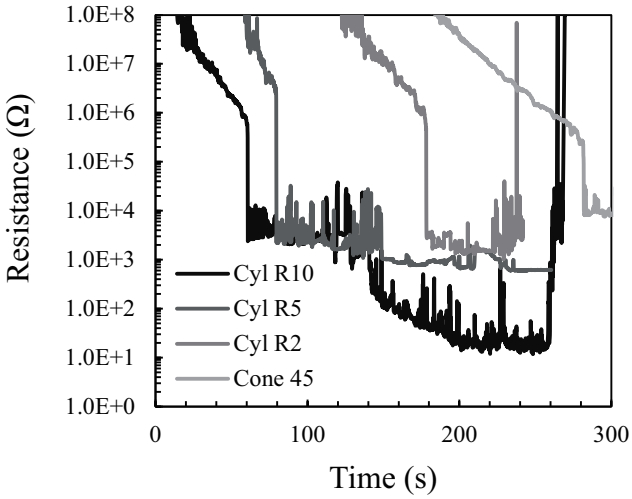

Figure 5.8: The electrical resistances for various intruders in solder balls. As the intruder size decreases, the electrical resistance curve shifts to the left side. Representative result for each case is shown ($n = 5$).

cylindrical intruder with diameter of 10 mm. Since rotation reduces the effective area where the granular hydrostatic pressure acts (see Fig. 5.4(b) and (c)), the electrical resistance curve shifts to left side as increasing the rotational speed (see Fig. 5.9(a)). We note that such shift is also shown in Fig. 5.8. We defined the onset of the sharp drop of the electrical resistance as the drop depth $l_d = t_d \times v$, where t_d is the onset time to begin to drop the electrical resistace and $v = 0.05$ mm/s is the thrusting velocity. As shown in Fig. 5.9(b), the average drop depth decreases with the rotational speed, which also indicates that rotational motion reduces the effective area where the granular hydrostatic pressure acts. Rotation breaks the force chains near the intruder, so that the formation of the current paths is delayed.

5.4 Conclusions

In this work, we provide a novel technique to observe the granular jamming by measuring the electrical resistance of granular medium consisting of the electrically conductive particles. We found that the electrical resistance

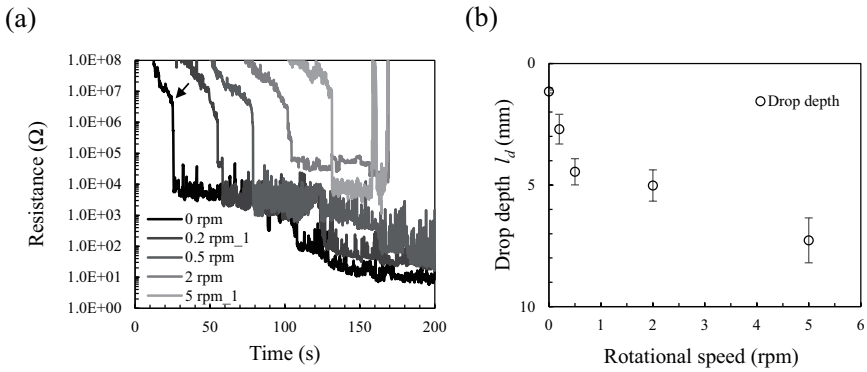

Figure 5.9: (a) The electrical resistances for the cylindrical intruder ($R = 10$) with rotation. The rotational speed ranges from 0.2 to 5 rpm. As the rotational speed increases, the electrical resistance curve shift to the left side. Representative result for each case is shown ($n = 3$). The black arrow indicates the onset of sharp drop of the electrical resistance. In this experiment, the height and diameter of the container filled with solder balls are 80 mm and 45 mm, respectively. (b) The average drop depth l_d ($n = 3$) according to rotational speed.

behavior during penetration of the intruder has three distinct regimes: no-contact, plastic deformation, and elastic deformation regimes, which show the real-time process of granular jamming under stress. We also observed the sharp drop of the electrical resistance, which represents various properties of granular system: the intruder size, grain heterogeneity, and the size of container filled with grains.

To validate this technique, we measured the vertical drag forces in solder balls medium, and compared with the electrical resistance of solder balls medium. In this experiment, we found that the sharp drop of the electrical resistance is delayed as decreasing the intruder size, indicating that granular jamming state is delayed as decreasing the intruder size. In a rotational experiment using glass beads, we see that the vertical drag force decreases with rotational speed and does not change in a linear dependence on the burial depth for the cylindrical intruder, which indicate that rotation reduces the effective area of the intruder where the granular hydrostatic pressure acts. We also measured the electrical resistance of solder balls medium while thrusting the intruder with rotation. The sharp drop of the electrical resistance also is delayed as increasing the rotational speed. We note that the relaxation of granular jamming by rotation can be easily observed by the measurement of the electrical resistance of solder balls medium. On the base of the intuitive physical knowledge of relaxation of the force chains by rotation, this work will give a new insight to granular mechanics and design of robots working in soils.

Chapter 6

Concluding remarks

6.1 Conclusions

In this thesis, we discovered the markedly effective stratiegies of drag reduction in digging of self-burrowing rotary seeds of *Pelargonium*. The seeds have humidity-responsive awn, which can create motion to dig into soil in a humid environment. Strikingly, their rotation greatly lowers the resistance of soil against penetration. This motivates us to study granular drag on a rotating body. We find a correlation for the drag reduction in terms of a relative slip motion of grains, leading to a mathematical model for the granular drag of a rotating intruder without complicated intergranular mechanics. To validate the slip motion induced by rotation, we newly provided a simple and effective method to investigate the granular jamming under the rotating intruder. Using the electrically conductive particles, we measured the electrical resistance of granular medium. The behavior of the electrical resistance of granular medium shows the internal jamming process , irrespective of the experimental conditions.

In chapter 2, we have provided physical accounts of hygroscopically driven botanical motion. We suggested that the observed rotational motion of *Pelargonium* awns in response to environmental changes in humidity is caused by the tilted arrangement of the microfibrils in the inner layer of the awn. We also presented experimental measurements of the mechanical

characteristics of *Pelargonium carnosum*'s awns that enable their seeds to dig into the soil. The extensional force of the awn can be estimated by a simple elasticity for a coiled spring. Although the soil resistance to the seed's penetration without spinning is larger than the extensional force of the awn spring, the rotation of the seed greatly lowers the soil's resistance. Our quantitative measurements of the thrust and torque generated by the awn's hygroscopic deformation, and the soil's resistance, with and without rotation, naturally led to the question of the detailed mechanism behind the seed-head's rotation giving rise to such dramatic decrease in the forces needed to advance the seed into the soil.

In chapter 3, we investigated the granular drag for the vertically penetrating intruder in quasi-static flow regime. To investigate various effects on granular drag, we experimentally measured the drag force acting on the intruder. Based on the experimental results, we found that the quasi-static drag force normally acts on the intruder surface, and depends on the submerged volume of the intruder. We also showed that the polydispersity of grains greatly increases the drag force due to the strong interlocking between the neighboring grains. In addition, the effects of the relative size ratio of the grain to the intruder on granular drag was investigated. The relative size affects the grain-scale fluctuation of the drag force. We revealed that although the intruder size is comparable with the burial depth, the drag force also acts on the intruder in quasi-static manner. Our work gives an explanation of the shape of small animals living beneath the ground, and provides the detailed parameters to design biomimetic robots working in soil.

In chapter 4, we have measured the granular drag against a vertically penetrating intruder with rotation, and found that the drag reduction of a rotating intruder is critically determined by the relative slip velocity of the grains. We developed an semi-empirical correlation for the drag reduction by the slip motion of the grains, which leads to a novel model for the drag of a rotating intruder. Our work rationalized the drag reduction of the self-burrowing seeds by rotation, which must be advantageous for the

survival for the plant. Our study illuminates the functionality and beauty of natural design, as well as provides new insights into the design of self-sustainable drilling robots for military and environmental applications and underground exploration in space. Visualization of the granular pressure distribution and the granular motion beneath the rotating intruder would further our understanding of drag reduction from a microscopic point of view.

In chapter 5, we suggested a novel technique to investigate the granular jamming process beneath the vertically penetrating rotary intruder using the electrically conductive particles. We measured the electrical resistance of granular medium consisting of the electrically conductive particles. We found that the electrical resistance decreases with the burial depth, and has three distinct regimes: no-contact, plastic deformation, and elastic deformation regimes. We also observed the sharp drop of the electrical resistance showing various properties of granular system. To validate this method, we measured the vertical drag forces in solder balls medium with rotation and without rotation, and compared with the electrical resistance of solder balls medium. We found that the sharp drop of the electrical resistance is delayed as increasing rotational speed, which is reminiscent with delaying the sharp drop by decreasing the intruder size. We note that the relaxation of granular jamming by rotation can be evaluated by measuring the electrical resistance of solder balls medium.

Inspired by the self-burrowing of the *Erodium* and *Pelargonium* seeds, this work presented the experimental study on how rotation during penetration can reduce the granular drag force. Experimental results show that the relative ratio of rotational speed to penetration speed determines the reduction magnitude of the granular drag force without change in the dependence on the burial depth. The proposed model captured the experimental results nicely, which successfully explains the drag reduction of the rotating intruders including self-burrowing rotary seeds. To validate the effect of rotation on granular drag, we provided a novel technique to investigate granular jamming under the penetrating intruder with rotation using

the electrically conductive particles, which are able to form the electrical current paths forced into contact. We expect that our work will excite the physicists in the field of granular mechanics. Moisture driven botanical motions will give us a window on self-actuators, and thus our study provides engineers with new insights into the design of self-sustainable drilling robots for military and environmental applications. Most importantly, the functionality and beauty of natural design of the self-burrowing seeds will be evidenced by our work.

6.2 Future work

In chapter 5, we provided a novel technique to investigate the granular jamming using the electrically conductive particles. We experimentally measured the electrical resistance of granular medium consisting of solder balls, and found that the behavior of the electrical resistance can be divided by three distinct regimes. Although we provided qualitative explanations for three regimes, the detailed micro-scale descriptions for the intergranular motions by the external shear are needed. Using a discrete elements method (DEM), we will visualize the formation of the force chains during penetration of the intruder with rotation and without rotation. With the simulation results, we will analyse the force chain networks, and calculate the electrical resistance of granular medium consisting of the electrically conductive particles under shear by applying Kirchhoff's law.

References

Abraham, Y. & Elbaum, R. (2013a). Hygroscopic movements in geraniaceae: the structural variations that are responsible for coiling or bending. *New Phytol.*, **199**, 584–594.

Abraham, Y. & Elbaum, R. (2013b). Quantification of microfibril angle in secondary cell walls at subcellular resolution by means of polarized light microscopy. *New Phytol.*, **97**, 1012–1019.

Abraham, Y., Tamburu, C., Klein, E., C., D.J.W., Fratzl, P., Raviv, U. & Elbaum, R. (2012). Tilted cellulose arrangement as a novel mechanisim for hygroscopic coiling in the stork's bill awn. *J. R. Soc. Interface*, **9**, 640–647.

Aharoni, H., Abrabam, Y., Elbaum, R., Sharon, E. & Kupferman, R. (2012). Emergence of spontaneous twist and curvature in non-euclidean rods: applicationi to *Erodium* plant cells. *Phys. Rev. Lett.*, **108**, 238106.

Albert, I., Tegzes, P., Kahng, B., Albert, R., Sample, J.G., Pfeifer, M., Barabási, A.L., Vicsek, T. & Schiffer, P. (2000). Jamming and fluctuations in granular drag. *Phys. Rev. Lett.*, **84**, 5122.

Albert, I., Sample, J.G., Morss, A.J., Rajagopalan, S., Barabási, A.L. & Schiffer, P. (2001a). Granular drag on a discrete object: shape effects on jamming. *Phys. Rev. E*, **64**, 061303.

Albert, I., Tegzes, P., Albert, R., Sample, J.G., Barabási, A.L. & Kahng, P., B Schiffer (2001b). Stick-slip fluctuation in granular drag. *Phys. Rev. E*, **64**, 031307.

Albert, R., Pfeifer, M.A., Barabási, A.L. & Schiffer, P. (1999). Slow drag in a granular medium. *Phys. Rev. Lett.*, **82**, 205.

Armon, S., Efrati, E., Kupferman, R. & Sharon, E. (2011). Geometry and mechanics in the opening of chiral seed pods. *Science*, **333**, 1726–1730.

Barnett, J.R. & Bonham, V.A. (2004). Cellulose microfibril angle in the cell wall of wood fibers. *Bil. Rev.*, **79**, 461–472.

Beer, T. & D., S.M. (1977). On the theory of explosively dispersed seeds. *New Phytol.*, **78**, 681–694.

Bengough, A.G. & Mullins, C.E. (1990). Mechanical impedance to root growth: a review of experimental techniques and root growth responses. *J. Soil. Sci.*, **41**, 341–358.

Bengough, A.G., Mullins, C.E. & Wilson, G. (1997). Estimating soil frictional resistance to metal probes and its relevance to the penetration of soil by roots. *Eur. J. Soil. Sci.*, **48**, 603–612.

Bertho, Y., Giorgiutti-Dauphiné, F. & Hulin, J.P. (2003). Dynamical janssen effect on granular packing with moving walls. *Phys. Rev. Lett.*, **90**, 144301.

Biroli, G. (2007). Jamming: a new kind of phase transition. *Nature Phys.*, **3**, 222–223.

Bocquet, L., Colin, A. & Ajdari, A. (2009). Kinetic theory of plastic flow in soft glassy materials. *Phys. Rev. Lett.*, **103**, 036001.

Brown, E. & Jaeger, H.M. (2009). Dynamic jamming point for shear thickening suspensions. *Phys. Rev. Lett.*, **103**, 086001.

Brzinski III, T.A. & Durian, D.J. (2010). Characterization of the drag force in an air-moderated granular bed. *Soft matter*, **6**, 3038–3043.

Brzinski III, T.A., Mayor, P. & Durian, D.J. (2013). Depth-dependent resistance of granular media to vertical penetration. *Phys. Rev. Lett.*, **111**, 168002.

Cates, M.E., Wittmer, J.P., Bouchaud, J.P. & Claudin, P. (1998). Jamming, force chains, and fragile matter. *Phys. Rev. Lett.*, **81**, 1841.

Chehata, D., Zenit, R. & Wassgren, C.R. (2003). Dense granular flow around an immersed cylinder. *Phys. Fluids*, **15**, 1622–1631.

Clark, A.H., Petersen, A.J., Kondic, L. & Behringer, R.P. (2015). Nonlinear force propagation during granular impact. *Phys. Rev. Lett.*, **114**, 144502.

Corwin, E.I., Jaeger, H.M. & Nagel, S.R. (2005). Structural signature of jamming in granular media. *Nature*, **435**, 1075–1078.

da Cruz, F., Emam, S., Prochnow, M., Roux, J.N. & Chevoir, F. (2005). Rheophysics of dense granular materials: discrete simulation of plane shear flows. *Phys. Rev. E*, **72**, 021309.

Desmond, K.W. & Weeks, E.R. (2015). Measurement of stress redistribution in flowing emulsions. *Phys. Rev. Lett.*, **115**, 098302.

Dumais, J. & Forterre, Y. (2012). "vegetable dynamicks": the role of water in plant movements. *Annu. Rev. Fluid Mech.*, **44**, 453–478.

Elbaum, R., Zaltman, L., Burgert, I. & Fratzl, P. (2007). The role of wheat awns in the seed dispersal unit. *Science*, **316**, 884–886.

Elbaum, R., Gorb, S. & Fratzl, P. (2008). Structures in the cell wall that enable hygroscopic movement of wheat awns. *J. Struct. Biol.*, **164**, 101–107.

Evangelista, D., Hotton, S. & Dumais, J. (2011). The mechanics of explosive dispersal and self-burial in the seeds of the filaree, *Erodium cicutarium* (genraniaceae). *J. Exp. Biol.*, **214**, 521–529.

Fenistein, D., van de Meent, J.W. & van Hecke, M. (2004). Universal and wide shear zones in granular bulk flow. *Phys. Rev. Lett.*, **92**, 094301.

Foreterre, Y., Skotheim, J.M., Dumais, J. & Mahadevan, L. (2005). How the venus flytrap snaps. *Nature*, **433**, 421–425.

Forterre, Y. & Pouliquen, O. (2008). Flows of dense granular media. *Ann. Rev. Fluid Mech.*, **40**, 1–24.

Franks, P.J., Buckley, T.N., Shope, J.C. & Mott, K.A. (2001). Guard cell volume and pressure measured concurrently by confocal microscopy and the cell pressure probe. *Plant Physiol.*, **125**, 1577–1584.

Fratzl, P., Elbaum, R. & Burgert, I. (2008). Cellulose fibrils direct plant organ movements. *Faraday Discuss.*, **139**, 275–282.

Gerbode, S.J., Puzey, J.R., McCormick, A.G. & Mahadevan, L. (2012). How the cucumber tendril coils and overwinds. *Science*, **371**, 1087–1091.

Guillard, F., Forterre, Y. & Pouliquen, O. (2013). Depth-independent drag force induced by stirring in granular media. *Phys. Rev. Lett.*, **110**, 138303.

Hepworth, D.G. & Vincent, J.F.V. (1998). The mechanical properties of xylem tissue from tobacco plants (*Nicotiana tabacum* 'samsun'). *Ann. Bot. Lond.*, **81**, 751–759.

Higashi, N. & Sumita, I. (2009). Experiments on granular rheology: effects of particle size and fluid viscosity. *J. Geophys. Res.*, **114**, B04413.

Hill, G., Yeung, S. & Koehler, S. (2005). Scaling vertical drag forces in granular media. *Europhys. Lett.*, **72**, 137–143.

Hinds, T.E. & Hawsworth, F.G. (2000). Seed dispersal velocity in four dwarfmistletoes. *Science*, **23**, 517–519.

Hosoi, A.G. & Goldman, D.I. (2015). Beneath our feet: strategies for locomotion in granular media. *Ann. Rev. Fluid Mech.*, **47**, 431–453.

Jaeger, H.M. & Nagel, S.R. (1996). Granular soilds, liquids, and gases. *Rev. Mod. Phys.*, **68**, 1259–1273.

Jeong, K.U., Jang, J.H., Kim, D.Y., Nah, C.N., Lee, J.H., Lee, M.H., Sun, H.J., Wang, C.L., Cheng, S.Z.D. & Thomas, E.L. (2011). Three-dimensional actuators transformed from the programmed two-dimensional structures via bending, twisting and folding mechanism. *J. Mater. Chem.*, **21**, 6824–6830.

Jung, S. (1987). *Caenorhabditis elegans* swimming in a saturated particulate system. *Phys. Fluids*, **22**, 031903.

Jung, W., Kim, W. & Kim, H.Y. (2014). Self-burial mechanics of hygroscopically responsive awns. *J. Fluid Mech.*, **311**, 219–237.

Kabla, A. & Debrégeas, G. (2003). Local stress relaxation and shear banding in a dry foam under shear. *Phys. Rev. Lett.*, **90**, 258303.

Katifori, E., Alben, S., Cerda, E., Nelson, D.R. & Dumais, J. (2010). Foldable structures and the natural design of pollen grains. *Proc. Natl. Acad. Sci. USA*, **107**, 7635–7639.

Landau, L.D. & Lifshitz, E.Z. (1970). Theory of elasticity. 2nd ed. *Pergamon Press (NY).*

Lee, A., Moon, M.W., Lim, H., Kim, W.D. & Kim, H.Y. (2005). Physical limits and design principle for plant and fungal movements. *Science*, **308**, 1308–1310.

Lee, M., Kim, S. & Kim, H.Y. (2016). Bending and buckling of wet paper. *Phys. Fluid*, **25**, 042101.

Li, C., Zhang, T. & Goldman, D.I. (2013). A terradynamics of legged locomotion on granular media. *Science*, **339**, 1408–1412.

Liu, A.J. & Nagel, S.R. (1998). Jamming is not just cool any more. *Nature*, **396**, 21.

Ma, M., Guo, L., Anderson, D. & Langer, R. (2013). Bio-inspired polymer composite actuator and generator driven by water gradients. *Science*, **339**, 186–189.

Majmudar, T.S., Sperl, M. & Behringer, R.P. (2007). Jamming transition in granular systems. *Phys. Rev. Lett.*, **98**, 058001.

Maladen, R.D., Ding, Y., Li, C. & Goldman, D.I. (2009). Undulatory swimming in sand: Subsurface locomotion of the sandfish lizard. *Science*, **325**, 314–318.

MiDi, G. (2004). On dense granular flows. *Eur. Phys. J. E*, **14**, 341–365.

Mueth, D.M., Jaeger, H.M. & Nagel, S.R. (1998). Force distribution in a granular medium. *Phys. Rev. E*, **57**, 3164.

Mueth, D.M., Debregeas, G.F., Karczmar, G.S., Eng, P.J., Nagel, S.R. & Jaeger, H.M. (2000). Signatures of granular microstructure in dense shear flows. *Nature*, **406**, 385–389.

Muthuswamy, M. & Tordesillas, A. (2006). How do interparticle contact friction, packing density and degree of polydispersity affect force propagation in particulate assemblies? *J. Stat. Mech.*, **9**, P09003.

Nawroj, A.I., Swensen, J.P. & Dollar, A.M. (2013). Electrically conductive bulk composites through a contact-connected aggregate. *Plos one*, **8**, e82260.

Ostojic, S., Somfai, E. & Bernard, N. (2006). Scale invariance and universalty of force networks in static granular matter. *Nature*, **439**, 058001.

Pandolfi, C. & Izzo, D. (2013). Biomimetics on seed dispersal: survey and insights for space exploration. *Bioinspir. Biomim.*, **8**, 025003.

Peters, J.F., Muthuswamy, M., Wibowo, J. & Tordesillas, A. (2005). Characterization of force chains in granular material. *Phys. Rev. E*, **72**, 041307.

Reddy, K.A., Forterre, Y. & Pouliquen, O. (2011). Evidence of mechanically activated processes in slow granular flows. *Phys. Rev. Lett.*, **106**, 108301.

Reyssat, M., Pardo, F. & Quéré, D. (2009). Drops onto gradients of texture. *Europhys. Lett.*, **87**, 36003.

Richard, P., Nicodemi, M., Delannary, R., Ribiére, P. & Bideau, D. (2005). Slow relaxation and compaction of granular systems. *Nature Mater.*, **4**, 121–128.

Roper, M., Seminara, A., Bandi, M.M., Cobb, A., Dillard, R. & Pringle, A. (2010). Dispersal of fungal spores on a cooperatively generated wind. *Proc. Natl. Acad. Sci. USA*, **107**, 17474–17479.

Sakaie, K., Fenistein, D., Carroll, T.J., van Hecke, M. & Umbanhowar, P. (2008). Mr imaging of reynolds dilatancy in the bulk of smooth granular flows. *Europhys. Lett.*, **84**, 38001.

Schall, P. & van Hecke, M. (2010). Shear bands in matter with granularity. *Annu. Rev. Fluid Mech.*, **42**, 67–88.

Seguin, A., Bertho, Y. & Crassous, J. (2011). Dense granular flow around a penetrating object: experiment and hydrodynamic model. *Phys. Rev. Lett.*, **107**, 048001.

Shinbrot, T. (2004). Granular materials: the brazil nut effect - in reverse. *Nature*, **429**, 352–353.

Soller, R. & Koehler, S.A. (2006). Drag and lift on rotating vanes in granular beds. *Phys. Rev. E*, **74**, 021305.

Stamp, N.E. (1984). Self-burial behaviour of *Erdium cicutarium* seeds. *J. Ecol.*, **72**, 611–620.

Stone, M.B., Baryy, R., Bernstein, D.P., Pelc, M.D., Tsui, Y.K. & Schiffer, P. (2004). Local jamming via penetration of a granular medium. *Phys. Rev. E*, **70**, 041301.

Swensen, J.P. & Dollar, A.M. (2012). The connectedness of packed circles and spheres with application to conductive cellular materials. *Plos one*, **7**, e51695.

To, K., Lai, P.Y. & Pak, H.K. (2001). Jamming of granular flow in a two-dimensional hopper. *Phys. Rev. Lett.*, **86**, 71.

Tordesillas, A., Steer, C.A.H. & Walker, D.M. (2014). Force chain and contact cycel evolution in a dense granular material under shallow penetration. *Nonlin. Processes Geophys.*, **21**, 505–519.

Trappe, V., Prasad, V., Cipelletti, L., Segre, P.N. & Weitz, D.A. (2001). Jamming phase diagram for attractive particles. *Nature*, **411**, 772–775.

Weintraub, M. (1952). Leaf movements in *Mimosa pudica* l. *New Phytol*, **50**, 357–382.

Wentworth, C.K. (1922). A scale of grade and class terms for clastic sediments. *J. Geol.*, **50**, 377–392.

White, F.M. (2006). Vicous fluid flow. 3rd ed. *Mc Graw-Hill*.

Winter, A.G., Deits, R.L.H. & Hosoi, A.E. (2012). Localized fluidization burrowing mechanics of *Ensis directus*. *J. Exp. Biol.*, **215**, 2072–2080.

Wu, X.I., Måløy, A., Ammi, M. & Bideau, D. (1993). Why hour glasses tick. *Phys. Rev. Lett.*, **71**, 1363.

Yu, P. & Behringer, R.P. (2005). Granular friction: a slider experiment. *Chaos*, **15**, 041102.

Zuriguel, I. & Mullin, T. (2008). The role of particle shape on the stress distribution in a sandpile. *Proc. R. Soc. A*, **464**, 99–116.

국 문 초 록

회전이 입자상 재밍에 미치는 영향: 회전하여 자가매립하는 씨앗에서 착안한 연구

서울대학교 공과대학원
기계항공공학부
정 원 종

요 약

본 연구에서는 회전하면서 자가매립하는 씨앗에서 착안하여 회전이 입자상 재밍에 미치는 영향을 알아보기 위한 실험과 결과 해석을 위한 수학적 모델링을 수행하였다. 자가매립하는 씨앗은 주변의 습도 변화에 따라서 반응하여 회전 운동을 하게 되고, 이를 이용해서 입자상 항력, 즉 토양으로부터 씨앗이 받는 항력을 감소시켜 자가매립을 용이하게 한다. 회전하는 물체가 입자상 물질 속으로 침투할 때, 회전에 의해 침투체 주변의 입자들이 미끄럼 운동을 하게 되고 이로 인하여 회전체 주변의 입자들이 이루고 있는 힘 사슬들을 재배열시켜 침투제가 받는 입자상 항력이 현저히 감소하는 것을 실험적으로 발견하였다. 또한, 침투체의 회전에 의한 입자들의 상대 미끄럼 속도를 이용한 수학적 모델링을 통하여 회전 속도에 따른 입자상 항력 감소를 해석하였다. 회전에 의한 입자들의 미끄럼 운동이 입자들이 이루고 있는 힘 사슬 네트워크를 완화시켜 입자상 항력이 감소된다는 것을 입증하기 위해 전기 전도성 입자를 이용하여

입자상 물질 내부의 재밍 과정을 전기 저항으로 측정할 수 있는 획기적이고 효과적인 방법을 제시하였다. 본 연구는 복잡합 입자상 역학을 고려하지 않아도 입자상 물질에서 국부적인 입자들의 재배열이 항력에 얼마나 큰 영향을 주는지에 대한 직관적인 이해를 제공할 뿐만 아니라, 입자상 물질 내부 또는 표면에서 거동하는 소형 로봇의 기동성 항샹을 위한 설계 사양을 제공할 수 있을 것으로 기대된다.

먼저, 본 연구의 착안점이 된 자가매립 씨앗에 대해서 소개하였다. 에로듐과 펠라고늄 씨앗은 주변 환경의 습도 변화에 따라서 변형하는 까끄라기라는 씨앗 부속물을 가지고 있으며, 까끄라기는 씨앗의 자가매립에 매우 중요한 역할을 하게 된다. 에로듐과 펠라고늄 까끄라기는 건조한 환경에서는 스프링과 같은 형태와 같이 나선형으로 꼬여 있으며, 습한 환경에서는 선형적으로 펴지게 된다. 이러한 까끄라기의 흡습성 변형은 까끄라기가 습도에 반응하는 층과 반응하지 않는 층으로 이루어진 이중층 구조로 이루어져있기기 때문이다. 더욱 자세히 살펴보면 습도에 반응하는 층을 이루고 있는 셀룰로즈 마이크로 피브릴이 특정한 각도를 이루며 기울여져 있기 때문에 나선형 변형을 하게 된다. 까끄라기의 습도에 따른 변형이 자가매립에 어떻게 사용되는 지를 알아보기 위해 까끄라기 변형에 의해서 발생하는 힘을 실험적으로 측정하고 이론적으로 분석하였다. 까끄라기의 나선형 변형은 미는 힘과 돌림 힘을 동시에 씨앗에 발생시켜 씨앗을 스스로 땅 속으로 파고 들어가게 한다. 까끄라기의 미는 힘은 간단한 스프링 탄성 모델로 예측할 수 있다. 까끄라기의 미는 힘이 땅 속으로 파고 들어가는데 부족하더라도 씨앗의 회전에 의해 토양으로부터 씨앗이 받는 항력이 감소되어 거친 토양도 씨앗이 파고들어

갈 수 있게 된다는 것을 실험적으로 규명하였다. 이를 통해 자가매립 씨앗의 회전은 생존을 위한 자연의 진화적 산물이라고 할 수 있다.

자가매립 씨앗의 회전이 입자상 항력을 감소시키는 이유를 물리적으로 규명하기에 앞서, 저속으로 입자상 물질에 침투하는 물체가 받는 항력에 대한 연구을 수행하였다. 침투체에 작용하는 입자상 항력은 관성 수 I로 결정된다. 관성 수 I는 침투체에 작용하는 동마찰력과 정마찰력의 비율로 정의되며 관성 수 I가 10^{-3}보다 작을 경우 입자들의 유동은 준정적 영역에 해당하고, 이 경우 물체가 받는 입자상 항력은 정마찰력이 지배적인 역할을 하게 된다. 입자상 물질로부터 받는 정마찰력은 입자상 정수압과 내부 마찰계수의 곱으로 표현할 수 있다. 정마찰력은 정의에 의해서 물체에 작용하는 수직힘과 마찰계수의 곱으로 표현되기 때문에 준정적 영역에서는 입자상 항력이 침투체에 수직으로 작용하게 된다. 이를 실험적으로 규명하였으며 침투체의 기하학적 형상으로부터 잠긴 깊이와 입자상 항력에 대한 스케일링 법칙을 도출하였다. 또한, 입자 크기의 다분산성과 입자와 침투체의 상대적 크기 비율이 입자상 항력에 어떠한 영향을 미치는 지를 실험적으로 알아보았다. 입자 크기의 다분산성이 클수록 입자상 항력이 증가하며, 입자와 침투체의 상대적 크기 비율은 마이크로 스케일에서 입자상 항력에 영향을 미치는 스틱슬립 현상에 영향을 미치게 된다.

다음으로, 침투체의 회전에 의한 입자상 항력 감소를 정량적으로 측정하고 수학적 모델링을 통해 해석하였다. 회전에 의한 입자상 항력 감소는 회전하면서 자가매립하는 씨앗의 생존에 중요한 역할을

하게 되며, 자가매립 씨앗의 회전은 씨앗 부속물인 습도에 반응하는 까끄라기의 나선형 변형에 의해 발생한다. 침투체의 회전은 침투체 주변의 입자들이 이루는 힘 사슬 네트워크를 재배열하여 입자상 물질 내부의 힘 분포를 완화시키는 역할을 하게 되고, 이로 인해 침투체가 받는 입자상 항력을 크게 감소시킨다. 이는 침투체의 회전이 입자상 항력, 즉 입자상 정수압이 작용하는 침투체의 유효면적을 감소시키는 것으로 이해할 수 있다. 이러한 항력감소를 회전에 의해서 발생하는 주변 입자들의 상대적인 미끄럼 속도를 이용하여 수학적으로 모델링하고 실험결과와 비교하였다. 본 연구는 입자상 물질 내부에서 회전하는 물체에 의해서 발생하는 입자상 유동역학을 직관적으로 이해하는데 기여할 뿐만 아니라, 입자상 물질 내부 또는 표면에서 거동하는 로봇을 설계하는데 있어 기동성 향상을 위한 기준 사양을 제공할 수 있을 것으로 기대된다.

마지막으로 회전에 의한 입자들의 미끄럼 운동, 즉 회전에 의한 입자들의 재배열을 검증하기 위하여 전기 전도성 입자를 이용한 내부 재밍과정을 측정할 수 있는 새로운 기법을 개발하였다. 입자상 재밍은 입자들 간의 접촉으로 이루어진 힘 사슬 네트워크에 의해서 결정된다. 입자상 물질 내부에서 재밍이 일어날수록 입자들의 접촉으로 이루어진 사슬 네트위크의 밀도가 증가하게 된다. 이러한 입자들의 네트워크는 전기 전도성 입자들을 이용할 경우 전류 통로로서 역할을 하게 되며, 전기 전도성 입자들로 이루어진 입자상 물질에 전압을 인가할 경우 재밍 정도에 따라서 전기 저항이 감소를 예상할 수 있다. 이러한 직관적고 물리적 이해를 바탕으로, 전기 전도성 입자인 솔더볼로 이루어진 입자상 물질에 물체를 침투시키면서 입자상 물질의 전기저항을 측정하였다. 침투체의 잠긴 깊이에 따라서

입자상 물질의 전기 저항은 감소하였다. 또한 침투체의 단면적이 작아질 경우, 전기 저항이 감소하기 시작하는 시점이 지연되는 것을 실험적으로 확인하였다. 침투체가 회전할 경우, 회전 속도가 빨라질수록 입자상 물질의 전기 저항 감소 시점이 지연되었으며, 이는 침투체의 단면적이 작아지는 것과 같은 양상을 가짐을 발견하였다. 즉, 회전에 의해서 입자상 항력, 또는 입자상 정수압이 작용하는 유효면적이 감소되는 것을 의미한다. 전기 저항을 통한 입자상 물질 내부의 재밍 과정을 측정할 수 있는 기법을 이용하면, 복잡한 입자상 재밍 현상을 보다 직관적으로 이해할 수 있게 될 뿐만 아니라 땅 속에서 스스로 유리한 방향을 찾아가는 굴착 로봇을 설계하는데 있어 기준 사양을 제공할 수 있을 것으로 기대된다.

주요어 : 입자상 물질, 입자상 항력, 재밍, 식물 운동, 자가매립 씨앗, 흡습성 물질
학 번 : 2013 - 30211